November 2016

# Thermodynamic and Dynamic Models for Directed Assembly of Small Ensembles of Colloidal Particles

Raghuram Thyagarajan

# THERMODYNAMIC AND DYNAMIC MODELS FOR DIRECTED ASSEMBLY OF SMALL ENSEMBLES OF COLLOIDAL PARTICLES

A Dissertation Presented

by

RAGHURAM THYAGARAJAN

Submitted to the Graduate School of the
University of Massachusetts Amherst in partial fulfillment
of the requirements for the degree of

DOCTOR OF PHILOSOPHY

September 2016

Chemical Engineering

# THERMODYNAMIC AND DYNAMIC MODELS FOR DIRECTED ASSEMBLY OF SMALL ENSEMBLES OF COLLOIDAL PARTICLES

A Dissertation Presented

by

RAGHURAM THYAGARAJAN

Approved as to style and content by:

David M. Ford, Co-chair

Dimitrios Maroudas, Co-chair

Peter A. Monson, Member

Anthony D. Dinsmore, Member

John Klier, Department Head
Chemical Engineering

# DEDICATION

*To my parents and all my teachers.*

# ACKNOWLEDGMENTS

It is imperative that I begin the acknowledgments by thanking all of my committee members individually. I thank my advisor Professor David Ford profusely for accepting me as his student to work on this exciting project. It has been a very challenging project (and it continues to be so) right from the outset and I have managed to accomplish what I have so far due to his constant guidance all along this journey. Right from the thermodynamics course in my first semester towards all the research and non-research related meetings that I have had with Prof Ford has been a valuable learning experience for me. The fact that I could stop by his office anytime for discussing research was one of the biggest assets I had as a graduate student.

I thank my co-advisor, Professor Dimitrios Maroudas for his constant encouragement and support on all the projects that I have worked with him. The analysis course taught by him in my first semester here was one of the most exciting classes I attended in graduate school. I always have been excited to learn the new ideas he proposed for integrating concepts from the material science world with the realm of colloidal assembly. I would like to thank Prof Maroudas for including me in all his research group presentations that prepared me for all the national meetings that I have attended for the past few years. In this regard, I should thank both my advisors for encouraging me to attend all the national meetings that has definitely helped me with my presentation skills.

I thank my chemical engineering committee member Professor Peter Monson for having taken a keen interest on my progress over these past few years. I thank him immensely for including me in his weekly group meetings during the semesters. It has been a very rewarding experience getting to discuss research, present and exchange

ideas during these meetings and it has certainly helped me in my research projects. I also would acknowledge him for having taught the Statistical Thermodynamics course, which has been the central theme of my thesis work. I would also like to thank Prof Monson for giving me the opportunity to work on the NSF DMREF project during my last summer here.

I have to acknowledge Professor Anthony Dinsmore from the Physics department first for his wonderful treatment of the Fundamentals of the Solid State Physics course. It was my first exposure to such an involved course in solid state physics and I thoroughly enjoyed his lectures and constant discussions related to the topic. I also thank him for his guidance related to my thesis project and other interesting ideas related to colloidal assembly problems.

This thesis has been a purely collaborative effort right from the beginning and I should primarily thank the National Science Foundation Cyber-Enabled Discovery Program (NSF-CDI) for their generous funding support throughout my graduate school stay. Our collaboraters include Professor Michael Bevan from Johns Hopkins, Professor Martha Grover from Georgia Tech and Professor Benjamin Shapiro from University of Maryland College Park. I wish to thank all these professors for all the telephone conferences that I have been involved in for almost three years during my PhD. It has been a valuable experience for me discussing with faculty from diverse backgrounds. I also wish to thank their graduate students Yuguang Yang (JHU) and Xun Tang(Georgia Tech) with whom I have worked closely on research projects.

I like to thank the members of the Ford Research Group (Goessmann 210) that includes Nicole Labbe, Ray Sehgal, Ashutosh Rathi and Vadim Varshavsky. Nicole truly represented the fun side of our group and I got to share the office with her for a little more than a year and those moments are always cherishable. Ray has been nothing less than a mentor for me right from the time I started working on this project. I have hit multiple roadblocks in my thesis work and Ray has always been

there to help me with understanding the problem and trying to find a solution. I thank him for his support and encouragement. I would like to thank Ashutosh with whom I have shared the office for more than three years now. Despite working on different projects, we have always kept up on discussing our research progress and exchanged ideas related to our work. He has been very helpful both during and outside work and I would like to thank him for his support all these years. I also would like to thank our latest member, Vadim Varshavsky with whom I have been having interesting discussions recently on density functional theory calculations.

I have to acknowledge the support of all the computational researchers in Goessmann, that include students from the groups of Professors Maroudas and Monson. I would like to thank John Edison, Lin Jin, Szu-Chia Chen, Mohammad Navaid Khan, Anish Desouza from Prof Monson's group and Lin Hu, Asanka, DD, Xu Han, Lin Du, Ashish Kumar and Mengxi Chen from Prof Maroudas' group. I would like to thank DD in particular for his unstinted support during all those tough times. I have had a great time with my fellow researchers in Goessmann over the past few years, not to mention the occasional cricket we played on the corridor by our room Goessmann 210.

I sincerely thank all the administrative staff (Marie, Amity, Maggie, Lauren, Jessica, and Anshalee) in the Chemical Engineering office in Goessmann for all their help and support during these past five years. I would like to thank Marie Wallace in particular for taking care of the graduate students right from the admission stage all the way up to graduation.

I wish to thank my batchmates for all the times we had spent together during our first semesters working on assignments and preparing for exams. I would like to mention Katrina Rieger in particular, with whom I not only worked a lot during my first year on coursework and preparing for exams, but I also ended up collaborating with her and Prof Jessica Schiffmann for modeling bacteria transport in cellulose

fibre mats. It has been fun working with her all these years and I thank her for those times. I have also collaborated with Prof Shelly Peyton and Lauren Jansen for modeling protein adsorption on surfaces and I would like to thank them for giving me the opportunity.

I have been involved in a lot of activities outside of work in the Amherst area these past five years and most of the credit goes to the Chemical Engineering Graduate Soceity (ChEGS). The ChEGS group has been highly active in organizing social events round the year and make sure the students (especially the internationals) feel at home right from the time they join the program here. I for one, certainly felt comfortable and a sense of belonging to the community, thanks to the efforts of the members involved in ChEGS. There are a lot of people with whom I have had great times and I just would like to mention that ChEGS Softball was my favourite pastime during the summers and it provided the best opportunity to meet and interact with department members and UMass community members in general.

I have spent good times with few friends like Sara, Aaron, Alyssa, Kerianne, Vivek, Vishnu, Pranav, and Kiran where we got to hangout for biking, ice skating(my newfound pastime), and other fun activities. I would also like to thank Suhasini Kishore with whom I have spent lot of time discussing research as well as other topics during her frequent visits from Stony Brook. I would like to thank another bunch of friends from the Electrical Engineering department. I have spent a lot of time with Arun, Vinay, Ashish (few of my roommates), Abhishek, Divyashri, and Priyanka and want to mention that I have had so much fun the past few years with these people.

Having flown thousands of miles away from my parents and family in India, it took a few months to settle down in a new country and environment. I however was very fortunte that I had my uncle Ganesh Ramachandran, aunt Smitha Radhakrishnan and their kids living in Boston. They have been my family and home here for the last five years and I can't thank them enough for what they have done over these years. I

had wonderful times with my little cousins Medha and Abhigyan everytime I visited them. I would also like to thank my cousin Dr. Radhika Subramaniam with whom I have had a lot of conversations related to graduate school and the academic world.

I wish to mention my aunt Dr. Sarala Gopalan, who has been in touch with me on a regular basis all these years while I was doing my PhD. She has been constantly looking after me, trying to keep my morale high through this up and down journey. I thank her profusely for her support and belief she has shown in me.

I owe everything I have accomplished so far and everything I will in the future to my parents. They have been supportive of my academic journey right from the time I began college more than a decage ago. Their constant encouragement is what has kept me going all these years and I seek their blessings in all my future endeavors. Both my sister Janani and I came to the US for graduate school in the same year and it was helpful to have each other as we were settling down. She has been a source of great support over these years. I also would like to acknowledge a lot of family members and friends back in India who wish and pray for my success all the time and I cannot thank them enough.

Finally, I wish to mention that I have always and will continue to have the blessings of my grandfather, Shri V. Ramachandran, who would have been very proud of my achievements.

# ABSTRACT

## THERMODYNAMIC AND DYNAMIC MODELS FOR DIRECTED ASSEMBLY OF SMALL ENSEMBLES OF COLLOIDAL PARTICLES

SEPTEMBER 2016

RAGHURAM THYAGARAJAN

B.E.(Hons.), BIRLA INSTITUTE OF TECHNOLOGY & SCIENCE PILANI

M.Tech., INDIAN INSTITUTE OF TECHNOLOGY MADRAS

Ph.D., UNIVERSITY OF MASSACHUSETTS AMHERST

Directed by: Professor David M. Ford and Professor Dimitrios Maroudas

Self and directed assembly of finite clusters (10 to 1000) of colloidal particles into crystalline objects is an emerging area of scientific interest that finds applications in manufacturing of photonic crystals and other meta-materials. Such assembly problems are also of fundamental scientific interest because they involve thermodynamically small systems, with a number of particles that is far below the bulk limit. Robust methods for assembling defect-free target structures will ultimately require reduced-dimension process models that link the particle-level dynamics of the colloids to the actuator states. We have developed a three-part strategy for developing such process models.

First, we employ diffusion mapping (DMaps), a machine learning technique, on raw trajectory data to identify slow, low-dimensional manifolds in the system dynamics. Second, we identify convenient observables, or order parameters (OPs), that

strongly correlate with low-dimensional DMap coordinates; this step may involve a feedback loop with the DMap process itself. Third, we use a Fokker-Planck or Smoluchowski formalism to build free energy and diffusivity landscapes in the OPs, which serve as our reduced-dimension process models. We have applied this technique to two model systems in this work. The first system comprises 32 silica particles, which interact via a temperature-tunable depletion interaction potential. This system shows transitions between an expanded and condensed phase when the pair interaction strength is changed by a few $k_BT$. The second system comprises 210 quasi-2D silica particles confined within quadrupole electrodes and the interaction strength, which is of the order of few $k_BT$, is tuned by an externally applied electric field. This system shows interesting features like the formation and annealing of polycrystalline microstructures as the magnitude of the applied field is changed. We systematically compare and contrast the DMap analysis on both these model systems. We construct an optimal control policy map in the low-dimensional DMap coordinates using dynamic programming. The free energy and diffusivity landscapes along with the control policy map is used to robustly assemble perfect colloidal crystals.

We have also examined the phase behavior of the depletion potential system via a histogram-based simulation approach. We conducted replica exchange Monte Carlo simulations of these small colloidal clusters and generated potential energy histograms for various levels of the osmotic pressure that controls the interaction strength. By carefully tuning the osmotic pressure, we observed bimodal distributions in the potential energy space, which is indicative of coexistence between fluid-like and solid-like configurations. Quantitative analysis of these histograms yield phase coexistence curves for these small clusters and we report comparisons with bulk colloidal phase diagrams.

# TABLE OF CONTENTS

# LIST OF FIGURES

**Figure** **Page**

# CHAPTER 1

# INTRODUCTION

## 1.1 Background & Objectives

Colloidal crystals are periodic lattice structures of micron-sized particles that are important for several technological and scientific applications. The periodic lattice spacing in these crystals are of the order of wavelength of visible light, enabling them to manipulate the flow of light and function as "semiconductors of light" or photonic crystals [1–3]. Other technological applications include devices such as optical fibres, nanoscopic lasers and advanced meta-materials [3] that require the fabrication of ordered and defect-free crystals. An example of photonic device containing small clusters of crystalline colloidal materials is shown in Fig. 1.1.

Self assembly and directed assembly are widely used methods for producing colloidal crystals. Self assembly refers to the spontaneous organization of the colloidal particles due to presence of a net attractive potential between them [4–8]. Directed assembly requires the presence of an external stimuli, like gravity, electric or magnetic or flow fields, or directing templates to facilitate the process [9–12]. One of the main limitations of these techniques is the formation of polycrystalline structures. The lack of control over the interaction strengths during the course of the assembly causes irreversible aggregation leading to defective structures that cannot be corrected. Careful design of these materials with a periodic structure free of defects require a detailed understanding of the system's equilibrium and dynamical properties.

The main objective of this thesis is to construct robust mathematical models describing the thermodynamics and kinetics of directed assembly of such materials in order to engineer defect-free colloidal crystals. Such mathematical models (in the form

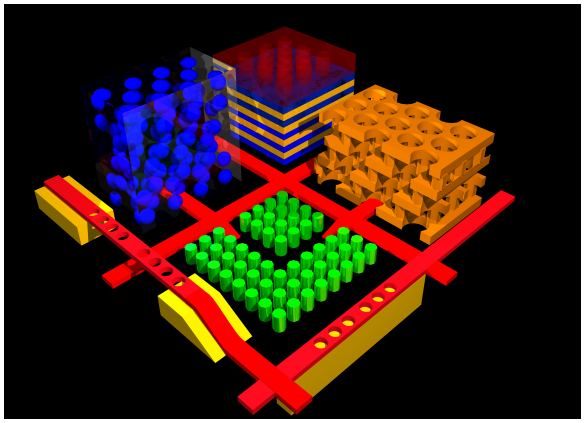

Figure 1.1: Photonic crystals containing finite clusters of dielectric material in a periodic lattice (from http://ab-initio.mit.edu/photons).

of free energy and diffusivity landscapes) can then be utilized in real-time feedback control to guide the directed assembly process and produce the desired target crystal structures. An important first step is understanding the thermodynamics of small colloidal clusters containing of the order of tens of particles. Such small clusters can serve as building blocks to engineer colloidal crystals for advanced meta-material applications. We have chosen to study two model colloidal systems in this thesis. The first system comprises colloidal silica particles in aqueous solution interacting via a temperature tunable depletion pair potential, details of which can be found in the literature [13–15]. The second system comprises colloidal silica particles confined within quadrupole electrodes to a monolayer due to gravitational forces. The pair potential interaction is controlled by means of an external electric field and more details on the experimental setup and the pair potential functions can be found in the literature [16–20].

In addition to having technological applications, such assembly problems are also of fundamental scientific interest because they involve thermodynamically small systems [21, 22], with the number of particles far below the bulk limit. These thermodynamically small systems exhibit phase behavior that is qualitatively different from

that of bulk materials [23]. For example, unlike bulk systems that have a fixed melting temperature at a given pressure, small clusters of atoms exhibit phase coexistence over a range of temperatures [24]. Phase coexistence can be dynamic in small systems, characterized by frequent transitions between phases whose relative free energy vary by a few $k_BT$, while for bulk systems, the slightest free energy difference is sufficient to constrain the system to the preferred phase. The second objective of this thesis it to explore the topic of small cluster phase behavior and compare and contrast the results with classical thermodynamics.

In order to build mathematical models, we have made use of the Fokker-Planck equation to desribe the stochastic behavior of the colloidal assembly. We require a convenient set of observables or order parameters to build Fokker-Planck models for which we have made use of a machine learning technique to determine the number and type of observables. Both of these techniques are described in the sections below.

## 1.2 Fokker-Planck Modeling Approach

The time evolution of systems displaying Markovian stochastic behavior is governed by the Fokker-Planck Equation (FPE). The FPE is a phenomenological conservation equation for the probability distribution in a set of observables [25–27] given by,

$$\frac{\partial \rho(\mathbf{\Psi}, t)}{\partial t} = L_{\mathrm{FP}}(\mathbf{\Psi}, t)\rho(\mathbf{\Psi}, t) \tag{1.1a}$$

$$L_{\mathrm{FP}}(\mathbf{\Psi}, t) \equiv \sum_{i=1}^{n} \frac{\partial}{\partial \psi_i} v_i(\mathbf{\Psi}, t) + \sum_{i,j=1}^{n} \frac{\partial^2}{\partial \psi_i \partial \psi_j} D_{ij}(\mathbf{\Psi}, t) \tag{1.1b}$$

where $L_{\mathrm{FP}}$ is the Fokker-Planck operator, $\mathbf{\Psi}$ is the vector of observables, $\rho(\mathbf{\Psi}, t)$ is the probability distribution function, $v_i$ is the drift coefficient of the $i^{\mathrm{th}}$ variable, and $D_{ij}$ is the $(ij)^{\mathrm{th}}$ element of the diffusion coefficient matrix which are directly related to the first two moments of $\mathbf{\Psi}$. The drift and diffusivity coefficients of the FPE can be extracted from a set of dynamic trajectories initiated in the observable or coarse variable space.

This technique of modeling stochastic systems has been extensively used to study the thermodynamics and kinetics of peptide fragment dissolved in water [28], micelle formation [29, 30], and stress-induced structural and order-disorder transitions in crystalline solids [31–33]. The central theme underlying all of this work is the assumption of an existence of a "slow manifold" parameterized by a set of "coarse-grained variables" or observables. The system dynamically evolves over this slow manifold and this technique provides a means for calculating the effective free-energy surface as a function of the coarse-grained variables.

The FPE can be suitably modified to describe a system of particles intercting via a conservative force-field $\mathbf{F}$ and the resulting equation is termed the Smoluchowski equation (SE) [34]. The connection between the FPE and the SE has been worked out elsewhere [35] and the SE for the evolution of the probability density $\rho(\mathbf{\Psi}, t)$ is given by,

$$\frac{\partial \rho(\mathbf{\Psi}, t)}{\partial t} = \bigtriangledown . \exp\left(-\frac{W(\mathbf{\Psi})}{k_B T}\right) \mathbf{D}(\mathbf{\Psi}) . \exp\left(\frac{W(\mathbf{\Psi})}{k_B T}\right) \rho(\mathbf{\Psi}, t) \tag{1.2}$$

where $W(\mathbf{\Psi})$ is the free energy landscape (FEL), $\mathbf{D}(\mathbf{\Psi})$ is the diffusivitiy landscape (DL), $k_B$ is Boltzmann constant, and $T$ is temperature.

For some systems, including the ones of interest here, the challenge in building the above mentioned Smoluchowski models lies in finding the appropriate number and type of coarse-grained variables. To this end we have used a machine learning technique discussed in the following section.

## 1.3 Diffusion Mapping: Coarse-Graining Approach

Diffusion map (DMap) analysis, sometimes referred to as the nonlinear analog of principal component analysis, provides a route to identifying low-dimensional representations of a high-dimensional data set [36–40].

In the context of colloidal assembly, data sets are typically generated from Brownian dynamics (BD) or Monte Carlo (MC) simulations. Consider for example, a simulation trajectory for a system containing $N$ particles. The data set generated from simulations comprises $3N$ particle coordinates describing the microstate of the system at each time instance or MC step. For a trajectory with $M$ snaphots, the total data is represented by a matrix with $M$ x $3N$ elements. The first step in DMap analysis is to compute the distance metric $d_{ij}$ between all pairs of snapshots $i, j = 1, 2, ...M$ in the data set. The choice of the distance metric is vital in synthesizing an effective low-dimensional manifold that captures the important modes of the process and this will be discussed later in this section.

Once the distance metric has been computed for all snaphot pairs, we compute the matrix $\mathbf{A}$ given by[41],

$$A_{ij} = \left(-\frac{d_{ij}^2}{2\epsilon}\right) \qquad i, j = 1, 2, ...M \tag{1.3}$$

where $\epsilon$ is a measure of the local neighborhood of any point in the data set. By construction, only data points that are separated by $d_{ij} \sim \sqrt{\epsilon}$ or smaller have a nonzero contribution in the matrix. A large value for $\epsilon$ implies all data points are connected while a small value implies only local connectivity. Suitable values for $\epsilon$ is provided by the extent of linear regime of in a plot of $\log(\sum_{i,j} A_{ij})$ against $\log(\epsilon)$ and twice the slope of the linear region provides an estimate of the dimensionality of the intrinsic manifold [42]. A Markov transition matrix $\mathbf{M}$ is constructed by normalizing the rows of $\mathbf{A}$ as shown below[41].

$$M_{ij} = \frac{A_{ij}}{\sum_{j=1}^{M} A_{ij}} \qquad i, j = 1, 2, ...M \tag{1.4}$$

Since $\mathbf{M}$ is a Markov matrix, the top eigenvalue and eigenvector is unity, *i.e.* $\lambda_1 = 1$ and $\nu_{1i} = 1, i = 1, 2, ...M$. The intrinsic dimensionality of the system is determined

by the presence of a spectral gap in the eigenvalue spectrum. A spectral gap after $\lambda_{k+1}$ implies a dimensionality of $k$, which is much lesser than the dimensionality of the problem $3N$ and $\lambda_2, \lambda_3, ...\lambda_{k+1}$ are the top $k$ non-trivial eigenvalues. The mapping of the $i^{\text{th}}$ snapshot into the $i^{\text{th}}$ components of each of the top $k$ non-trivial eigenvectors of the Markov matrix $\mathbf{M}$ is termed as the diffusion map embedding [41].

$$\text{snapshot}_i \rightarrow (\nu_2(i), \nu_3(i), ...\nu_{k+1}(i)) \tag{1.5}$$

While DMap analysis provides a value of $k$ and corresponding set of reduced-space coordinates for each data point in the set, it does not provide an explicit mapping between the $3N$-dimensional and $k$-dimensional coordinates. The task of identifying useful coarse variables in the $3N$-dimensional space requires some empiricism.

A simple illustration of the application of DMap technique to a Swiss roll data set is shown in Fig. 1.2. The data set shown in Fig. 1.2(a) comprises points residing in a 2D surface in 3D space. The distance metric $d_{ij}$ for this case is simply the Euclidean distance in $\mathcal{R}^3$. The DMap technique is able to recover the underlying intrinsic manifold of this data set as shown in Fig. 1.2(b) where the data is projected onto the $\nu_2 - \nu_3$ space.

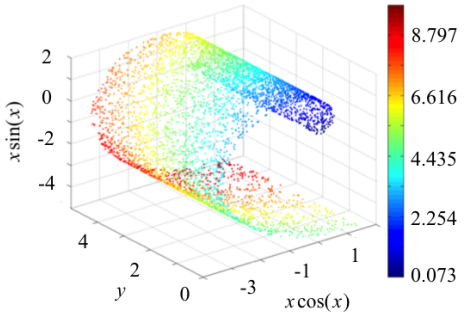


(a) Swiss roll data set with data points residing in a 2D surface in 3D space. The points are colored by their geodesic distance along the sprial.

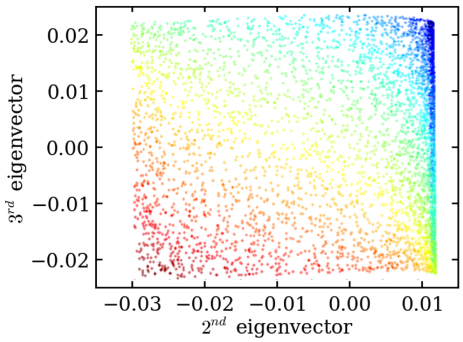


(b) Projection of the three dimensional data onto the top two eigenvectors $\nu_2 - \nu_3$ space recovers the underlying intrinsic manifold of the original data.

Figure 1.2: Illustration of the DMap technique to the Swiss roll data set.

However for assemblies of particles, we require a more sophisticated distance metric to capture transitions between microstates in the trajectory data set. We have used the Hausdorff distance metric to calculate distances between sets of points (coordinates of the particles in the clusters) in 3D space [43]. Let $C_1$ and $C_2$ denote two configuration snaphots and $C_1(i)$ denotes the position of particle $i$ in $C_1$. Hausdorff distance is defined as the maximum distance of a set to the nearest point in the other set and is given by [40],

$$d(C_1, C_2) = \max \left\{ \max_i \min_j \parallel C_1(i) - C_2(j) \parallel, \max_i \min_j \parallel C_2(i) - C_1(j) \parallel \right\} \quad (1.6)$$

Each of the two quantities inside the braces in Eq. 1.6 is the directed Hausdorff metric and it is an asymmetric function. The Hausdorff distance is computed as the maximum of the two directed Hausdorff metrics. Before the computation of the Hausdorff distance metric, each of the snapshots in the trajectory data set is mean centered, and aligned along their principal axes of inertia. This preprocessing step is carried out to make sure the distance metric computed is invariant under simple

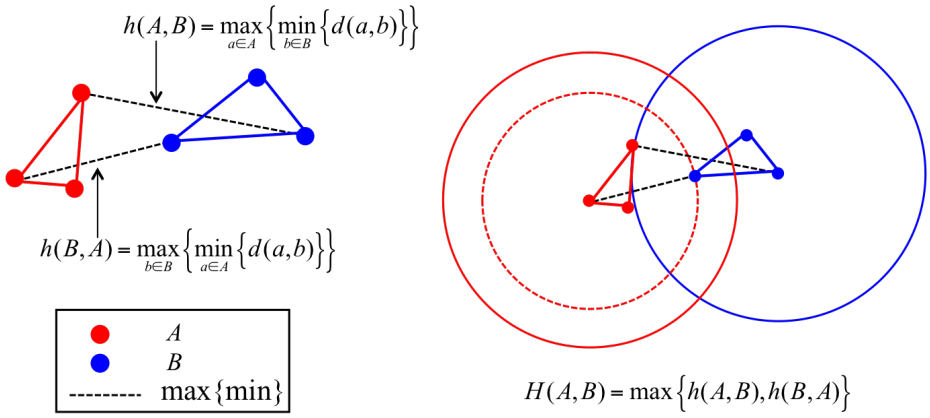


Figure 1.3: Hausdorff distance metric calculation for two polygons. $h(A, B)$ is the directed Hausdorff distance metric from set $A$ to $B$. The radius of the two solid circles (which are equal) is the Hausdorff distance metric and each point in one set is located at a distance that is at most equal to the Hausdorff distance from the other set.

translations and rotations of the snapshots [40]. This ensures that the DMap analysis captures only the underlying dynamic behavior of the system and not any degrees of freedom associated with translations and rotations. A simple application of the Hausdorff metric to a set of points is shown in Fig. 1.3.

The underlying assumption behind the use of DMap technique to find slow coarse variables is the fact that the system dynamics can be modeled as a diffusion process, whereby its evolution is restrained to an intrinsic manifold parameterized by a handful of coarse-variables, while all other degrees of freedom are effectively slaved to these slow modes. Diffusion mapping has been applied to model the evolution of complex biophysical systems like chain dynamics in solvents and protein folding problems [44, 45] to determine suitable order parameters. We will apply this technique for the assembly of small clusters of colloidal particles to identify the appropriate order parameters for building the low-dimensional Smoluchowski models.

## 1.4 Thesis Outline

This dissertation document is organized as follows. Chapter 2 begins with an introduction to the depletion potential system and discusses the existing Smoluchowski model built previously by our coworkers. It also contains the new coarse-grained model built using the bootstrapped DMap approach, the corresponding landscape models (FELs and DLs) and also the Markov state models and control policy maps built by our collaboraters. Chapter 3 begins with an introduction to the electric field (quadrupole) system and discusses the DMap results and the limitations of the distance metric used. We present a modified implementation of DMap with a new distance metric and present the landscape models (FELs and DLs) in the justified coarse-variable space. We also present some calculations performed by our collaboraters to benchmark the low dimensional models. In contrast to the Fokker-Planck order parameter approach presented in Chapters 2 and 3, Chapter 4 examines phase changes in small colloidal clusters by examining potential energy histograms. We revisit the depletion potential system here and present a quantitative analysis of phase coexistence in small clusters by analyzing histograms from replica exchange Monte Carlo simulations and compare them to predictions made from FELs. Finally, Chapter 5 summarizes the main findings of this thesis and also includes some future research directions related to this thesis and preliminary calculations for few of the topics discussed.

# CHAPTER 2

# COARSE-GRAINED LANDSCAPE MODELS: DEPLETION POTENTIAL SYSTEM

## 2.1 Introduction

We investigate the phase behavior of a system of silica particles $\sim 2\ \mu$m in diameter as the main colloidal species and $\sim 200$ nm in diameter poly-N-isopropylacrylamide (PNIPAM) gel particles as the depletant. The presence of the depletants in the solution results in a net attractive force between the silica particles through an entropic mechanism that was originally described by Asakura and Oosawa(AO) [46]. Fig. 2.1(a) shows the image of the silica particles in the presence of depletants and the corresponding pair potential interaction is shown in Fig. 2.1(b).

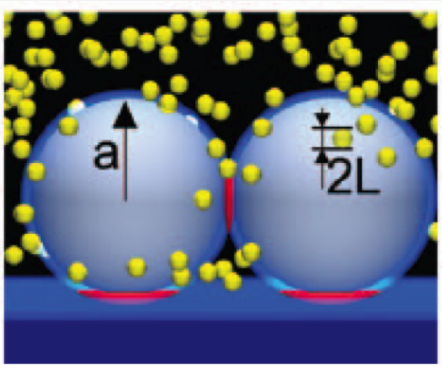


(a) Colloidal silica particles (blue spheres) with PNIPAM depletants (yellow spheres) in aqueous solution. The red zone is excluded volume between the colloids [15].

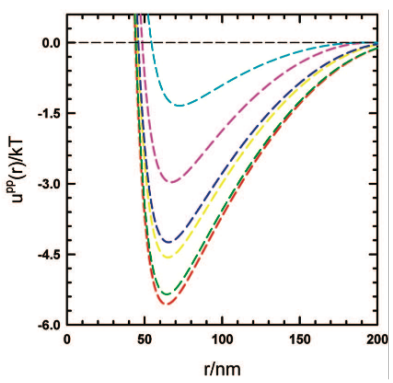


(b) The depth of the attractive pair potential between the colloids varies by a few $k_BT$ for the temperature range $T = 20$ °C - 29 °C [14].

Figure 2.1: Depletion potential system with its corresponding pair potential interaction.

The pair potential comprises an electrostatic double layer repulsion term and a temperature dependent attractive depletion potential. The attractive potential is well modeled by the AO expression with excluded volume and osmotic pressure terms [14, 15] and the total potential energy is given by

$$u_{\mathrm{tot}}^{\mathrm{pp}}(r_{ij}) = u_{\mathrm{E}}^{\mathrm{pp}}(r_{ij}) - \Pi\pi\left[\frac{4}{3}(a+L)^3\left(1 - \frac{3r_{ij}}{4(a+L)} + \frac{r_{ij}^3}{16(a+L)^3}\right)\right] \tag{2.1}$$

where $u_{\mathrm{E}}^{\mathrm{pp}}$ is the electrostatic respulsion term, $a$ is the colloidal silica radius, $L$ is the radius and $\Pi$ is the osmotic pressure of the depletants. It should be mentioned here that the effective one component pair potential model in Eq. 2.1 can accurately capture the experimental behavior when used in BD or MC simulations [14, 15]. The osmotic pressure $\Pi$ is modeled using the Carnahan-Starling hard sphere equation of state as [47],

$$\Pi = nk_BT\left[\frac{1+\phi+\phi^2-\phi^3}{(1-\phi)^3}\right] \tag{2.2}$$

where $n$ is the depletant bulk number density and $\phi$ is the depletant volume fraction

$$\phi = n\frac{4}{3}\pi L^3 \tag{2.3}$$

The quantity $\Pi$ is proportional to the volume fraction of solution occupied by the depletant species and therefore proportional to $L^3$, the cube of the depletant radius. The radius $L$ of the depletant particles (which also controls the range of the potential) is highly sensitive to temperature in the neighborhood of 25 °C, and minor changes in temperature can cause large changes in $\Pi$. Fig. 2.1(b) shows theoretical curves for the pair potential in Eq. 2.1 (obtained via inverse MC analysis) for temperatures varying between 20 °C (red curve) and 29 °C (cyan curve). It should be noted that $\Pi$ can also be controlled by varying the concentration of the depletants $n$ in the solution.

Depletant density $n$ affects the depth of the interaction while temperature $T$ affects both the depth and range of the attractive potential via the parameter $L$ and either of the two variables could be changed independently to control the osmotic pressure strength. The osmotic pressure values reported in this thesis are non-dimensionalized as $\Pi^* = \Pi a^3/k_BT$ where $k_BT/a^3$ is the scale for $\Pi$ in this system.

The particular system of interest in this study is a 32-particle cluster of the large colloidal particles. Fig. 2.2 shows the evolution of potential energy of these clusters in a BD simulation in the canonical ensemble in a cubic simulation box of volume fraction $\phi = 0.0695$ with periodic bounday conditions for $\Pi^* \sim 148$. The magnitude of $\Pi^*$ can be tuned to favour fluid or crystalline configurations [48]. For $\Pi^* \sim 148$ where the pair potential energy at equilibrium separation is $\sim$ -4.35 $k_BT$, we observe a transition at $t \sim 3000$ s from an expanded fluid-like phase to a solid-like phase. This is an interesting feature of the depletion potential system and we wish to probe this "crystallization" process in small colloidal clusters via the use of diffusion mapping technique. BD or MC simulations serve as the engine for producing large amounts of trajectory data sets which are the input for diffuion maps.

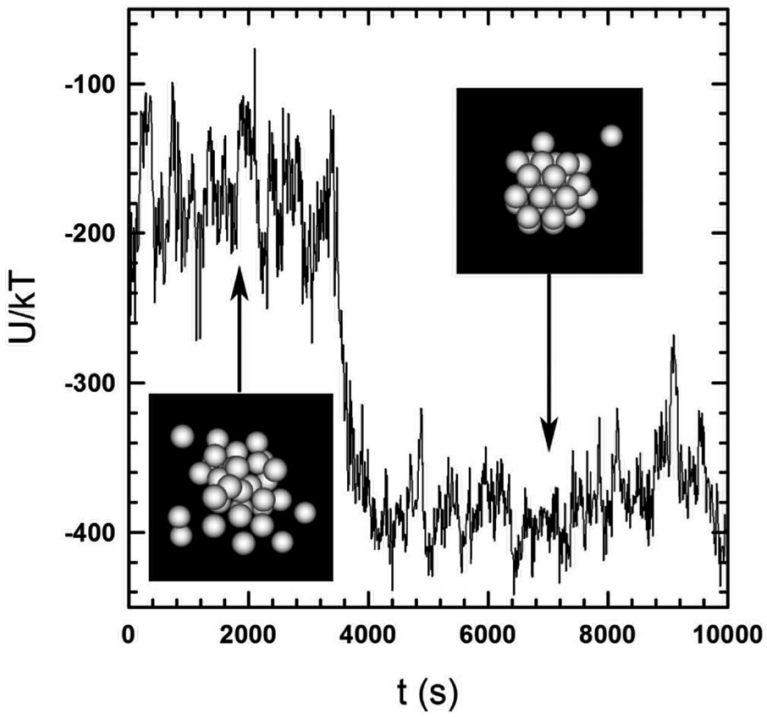


Figure 2.2: Evolution of potential energy, $U$, of a 32 particle cluster from a BD simulation. The insets show two configuration snapshots at different times in the trajectory marked by arrows. A transition is observed from a fluid-like to a solid-like state around $t \sim 3000$ s. Simulations were carried out in the canonical ensemble in a cubic box with periodic boundary conditions with a volume fraction $\phi = 0.0695$ and $\Pi^* \sim 148$ [49].

## 2.2 Coarse-Grained Smoluchowski Models

Previously, our coworkers have modeled the colloidal crystallization dynamics using both a 1D and 2D Smoluchowski model [49, 50]. The set of independent variables in the 2D Smoluchowski model was chosen using the technique of diffusion mapping (described in section 1.3) plus a heuristic analysis. The diffusion mapping technique indicated that two coarse variables would be sufficient. Numerous order parameter candidates were screened for use in constructing the model which included coordination number, cluster size, local and global orientational metrics. The final pair chosen was radius of gyration, $R_g^*$ to capture condensation and average number of hexagonally close packed neighboring particles, $\langle C_6 \rangle$ to capture crystallinity. Both $R_g^*$ and

$\langle C_6 \rangle$ showed the largest percent change with cyrstallization [48]. Fig. 2.3 shows two different snapshots with their $R_g^*$ and $\langle C_6 \rangle$ values. The radius of gyration, $R_g^*$, for $N$ particles of radius $a$ with position vector $\mathbf{r}$ is given by

$$R_g^* = \frac{1}{aN} \left[ \frac{1}{2} \sum_{i,j} |\mathbf{r}_i - \mathbf{r}_j|^2 \right]^{1/2} \tag{2.4}$$

where the $(*)$ denotes normalization by the particle radius.

The crystallinity order parameter, $\langle C_6 \rangle$, is defined as the average number of crystalline neighbors around each particle in an ensemble. The number of coordinated neighbors, $N_C(i)$, to particle $i$ are all particles $j$ within a coordination radius, $r_C$. Identification of crystalline nearest neighbors is based on a local sixfold orientational order parameter for the particle $i$ given by [51]

$$\bar{q}_{6m}(i) = \frac{1}{N_C(i)} \sum_{j=1}^{N_C(i)} Y_{6m}(\hat{\mathbf{r}}_{ij}) \tag{2.5}$$

where $\hat{\mathbf{r}}_{ij}$ is a unit vector specifying the orientation of the vector $\mathbf{r}_{ij}$ joining neighboring particles $i$ and $j$, and $Y_{6m}(\hat{\mathbf{r}}_{ij})$ are spherical harmonic components. The above equation can be normalized as

$$\tilde{q}_{6m}(i) = \frac{\bar{q}_{6m}(i)}{\left[ \sum_{m=-6}^{6} |\bar{q}_{6m}(i)|^2 \right]} \tag{2.6}$$

which is used to determine the crystalline connectivity, $\chi_6(ij)$, between particle $i$ and neighboring particles $j$ as

$$\chi_6(ij) = \sum_{m=-6}^{6} \tilde{q}_{6m}(i) \tilde{q}_{6m}(j)^* \tag{2.7}$$

where $\tilde{q}_{6m}(j)^*$ is the complex conjugate of $\tilde{q}_{6m}(j)$. The number of crystalline near neighbors, $C_6(i)$, for particle $i$ is

$$C_6(i) = \sum_{j=1}^{N_C(i)} \begin{bmatrix} 1 & \chi_6(ij) \geq 0.5 \\ 0 & \chi_6(ij) < 0.5 \end{bmatrix} \tag{2.8}$$

which gives the value of $\langle C_6 \rangle$ as the average over all particles in an ensemble as

$$\langle C_6 \rangle = \frac{1}{N} \sum_{i=1}^{N} C_6(i) \tag{2.9}$$

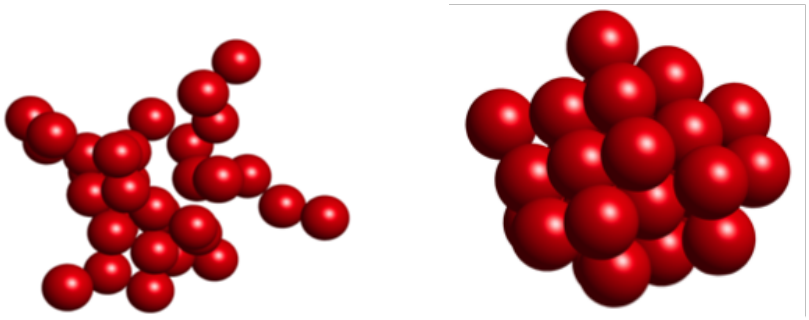

(a) Fluid-like configuration with $R_g^* = 4.05, \langle C_6 \rangle = 0.56$.

(b) Solid-like configuration with $R_g^* = 2.85, \langle C_6 \rangle = 6.88$.

Figure 2.3: Configuration snapshots shown along with their order parameter values $R_g^*$ and $\langle C_6 \rangle$.

The data set used for DMap analysis was produced using BD simulations at $\Pi^* \sim 148$ in the canonical ensemble. The data set contained 8000 snapshots that included both fluid-like and crystalline configurations. The eigenvalue spectrum for this data set shown in Fig. 2.4 indicates a spectral gap after the third non-trivial eigenvalue which implies that the system dynamics can be described with at most three dimensions in the Smoluchowski model.

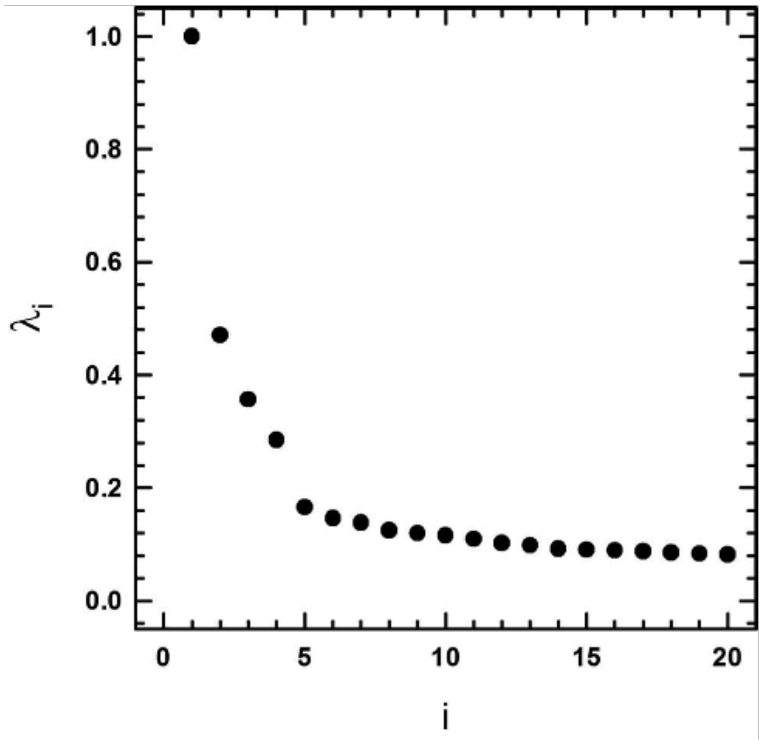


Figure 2.4: Eigenvalue spectrum shows a spectral gap after the third non-trivial eigenvalue $\lambda_4$ indicating a dimensionality requirement of at most three for this process [49].

The data set was examined in the top three non-trivial eigenvector coordinates as shown in Fig. 2.5. The BD data is plotted in diffusion map coordinate space, $\nu_2$, $\nu_3$, and $\nu_4$ and Figs. 2.5(a) and 2.5(d) show that the data essentially lie on a 2D manifold, which implies that a 2D Smoluchowski model is sufficient to model the dynamics. The correlations of the candidate order parameters $R_g^*$ and $\langle C_6 \rangle$ against the top eigenvectors were studied. The plots colored by $R_g$ (top row of Fig. 2.5) show that $R_g$ is some function of diffusion-map coordinates $\nu_2$ and $\nu_4$. This correlation is best observed only for the values of $R_g^* > 3.6$ where the data points lie on a nearly one dimensional manifold in the $\nu_2 - \nu_4$ space. However for lower $R_g^*$ values, there is no correlation with any of the diffusion mapping coordinates

The plots colored by $\langle C_6 \rangle$ (bottom row of Fig. 2.5) show a good clustering of high and low $\langle C_6 \rangle$ valued points. Low $\langle C_6 \rangle$ values are confined to the a small region in the

$\nu_2 - \nu_4$ space where there is some correlation. For $\langle C_6 \rangle > 1.5$ there is no correlation with any of the diffusion mapping coordinates. To summarize, no significant correlations were observed for both $R_g^*$ and $\langle C_6 \rangle$ against any of the DMap coordinates. This necessitated a search for alternate coarse-variables to build the low dimensional Smoluchoswski models. In the following section, we discuss a robust procedure to generate data sets and validate the choice of order parameters.

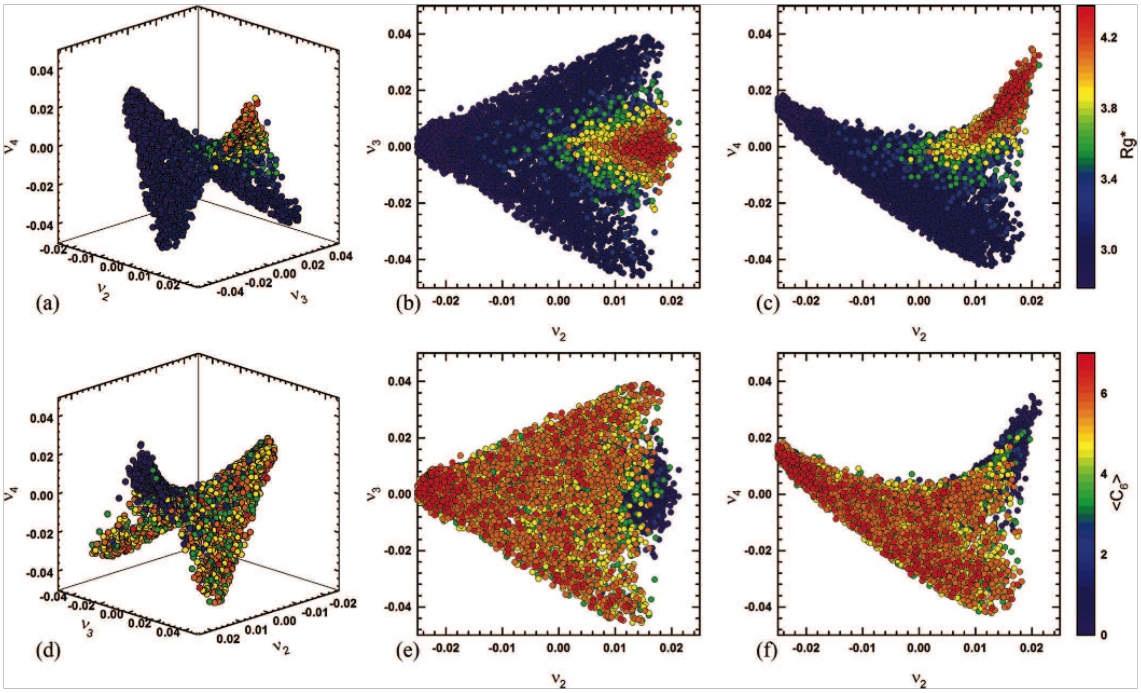


Figure 2.5: Different views of BD simulation data points plotted in the space of top three non-trivial eigenvectors $\nu_2$, $\nu_3$, $\nu_4$. The top row is colored by $R_g^*$ and the bottom row is colored by $\langle C_6 \rangle$ [49].

## 2.3 Diffusion Mapping: Bootstrapped Approach

Here we have adopted the idea of integrating diffusion mapping with Monte Carlo umbrella sampling (MC-US) as proposed by Ferguson and coworkers [44]. The umbrella sampling ensures a more complete coverage of the phase space, although the biased nature of the sampling must be accounted for when preparing the trajectory data set for the DMap analysis. We implemented the method as follows.

We choose $R_g^*$ and $\langle C_6 \rangle$ as the starting order parameter set. As explained in the previous section, this order parameter pair was used in constructing the intial model and serves as a reasonable starting point. We also employed the specific attraction strength value $\Pi^* = 147.74$ because this value is known to produce the most complex free energy landscape, with local minima representing both fluid-like and crystalline-like states. We carried out umbrella sampling on a grid spacing of (0.01, 0.0625) in the OP space $\psi = (R_g^*, \langle C_6 \rangle)$. Partially overlapping windows with side length equal to 10 times the grid spacing were used to cover the OP space, with hard walls used to constrain the system within a window during an MC run. We ran 50 million Monte Carlo steps per window and, by stitching together the free energy profiles in adjacent windows, produced a free energy landscape (FEL), $F(\psi)$, at the resolution of the grid. From this process we also naturally obtained a large collection of detailed particle configurations, or snapshots, that span the range of $\psi$. We then associated with each snapshot a Boltzmann weight given by

$$P(\psi_i) = \frac{e^{-\beta\psi_i}}{\Sigma_i e^{-\beta\psi_i}} \tag{2.10}$$

We used two-dimensional interpolation on the grid to compute each $F(\psi_i)$. Under this probability distribution, we scaled up our data set using

$$c_i = \text{round}([sP(\psi_i)]) \tag{2.11}$$

where $s$ is a scaling factor and $c_i$ is the multiplicity of each snapshot $i$. In the data set, each snapshot was then replicated a number of times equal to $c_i$ (essentially $c_i = 0$ removes that snapshot from the data set). This procedure transformed the inherently biased set of snapshots from MC-US into a set that is consistent with what an unbiased MC walk would have produced, assuming that the underlying choice of coarse variables provides a meaningful FEL. We set the scaling factor $s = 10^6$ and

subsampled to generate a data set containing $\sim 10^4$ snapshots. We employed this pseudo-unbiased set of snapshots as the input to the DMap analysis.

## 2.4 Diffusion Mapping Analysis: Dimensionality & Order Parameters

We analyzed three data sets obtained through the bootsrapped approach; one master data set that included both fluid-like and crystalline configurations; one subset included only those snapshots located in the fluid-like well on the FEL, and the other included only those snapshots located in the solid-like well. This new approach led us to discover a new order parameter that correlated much better with the diffusion mapping coordinates than what was observed with the BD data set discussed earlier. We introduce the new order parameter in the next section and follow it up with the diffusion mapping results.

### 2.4.1 Average Cluster-Cluster Distance Metric

In addition to $R_g^*$ and $\langle C_6 \rangle$, we introduce $D_{cc}^*$, a third order parameter which is defined as the average pairwise distance between distinct clusters in the system normalized by the radius of a single particle. A cluster is defined as a subset of particles that are mutually connected by pairwise bonds. A pair of colloidal particles is defined as bonded if they are close enough to experience the mutual attractive entropic interaction caused by the depletant particles and that distance is 2.2 (radii units) for the system being studied. The number of distinct clusters in an $N$-particle system may range from 1 to $N$ ($N = 32$ here). The pairwise distance between two clusters is defined as the smallest distance between any pair of particles, with the pair comprising one particle from each cluster. In the case of only one distinct cluster, $D_{cc}$ is set to a value that corresponds to the maximum bonded length for a particle pair; this makes $D_{cc}^*$ an essentially continuous function with a lower bound equal to the

maximum bonded length. As an example, Fig. 2.6 shows two configuration snapshots, a single cluster and a broken one. Both $R_g^*$ and $\langle C_6 \rangle$ show minor differences between the two snaphots but $D_{cc}^*$ is able to quantify the effect of broken clusters significantly. We test the correlations of the non-trivial eigenvectors against all the three order parameters.

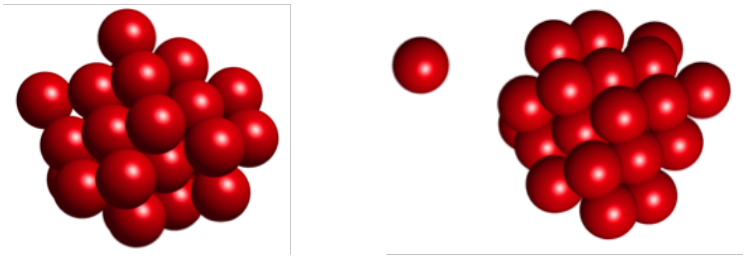

(a) Solid like configuration with $R_g^* = 2.85, \langle C_6 \rangle = 6.88, D_{cc}^* = 2.20$. $D_{cc}^*$ is set to a maximum bonded length value for a single cluster.

(b) Broken cluster configuration with $R_g^* = 2.96, \langle C_6 \rangle = 6.32, D_{cc}^* = 4.40$. $D_{cc}^*$ shows a significant change for clusters with broken fragments.

Figure 2.6: Configuration snapshots shown along with their order parameter values $R_g^*$, $\langle C_6 \rangle$, and $D_{cc}^*$.

### 2.4.2 Data Sets

The first step towards generating data sets involve construction of the FEL in the chosen OP space $\psi = \left(R_g^*, \langle C_6 \rangle\right)$. The FELs for three different osmotic pressures are shown in Fig. 2.7. Fig. 2.7(a) is the FEL at $\Pi^* = 139.76$ where a basin at high $R_g^*$ and low $\langle C_6 \rangle$ is the only stable fluid-like phase. At a higher value of $\Pi^* = 147.74$, a more stable crystalline-like solid phase emerges at low $R_g^*$ and high $\langle C_6 \rangle$ and the fluid-like phase is metastable as shown in Fig. 2.7(b). The FEL for the highest osmotic pressure $\Pi^* = 173.03$ is shown in Fig. 2.7(c) and the only basin at high values of $\langle C_6 \rangle$ is the crystalline-like solid phase. As mentioned before, since the intermediate value of $\Pi^*$

captures the coexistence of fluid-like and solid-like phases, the corresponding FEL in Fig. 2.7(b) is chosen to generate the data sets.

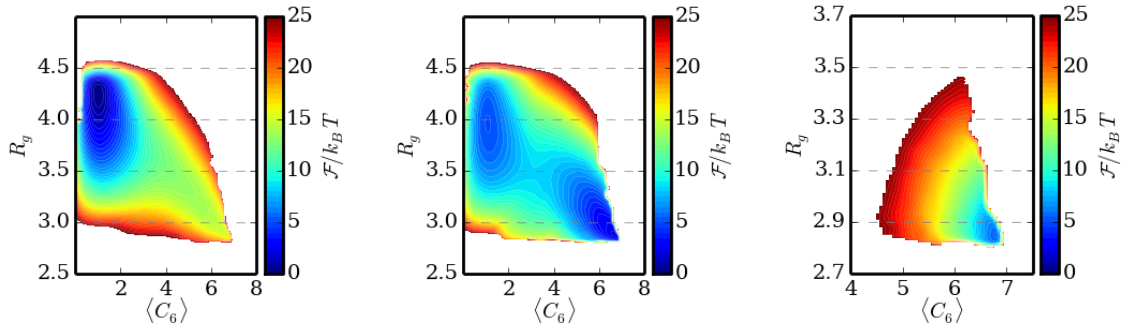


(a) $\Pi^* = 139.76$ (b) $\Pi^* = 147.74$ (c) $\Pi^* = 173.03$

Figure 2.7: FELs in $R_g^* - \langle C_6 \rangle$ space for three osmotic pressures $\Pi^*$. These FELs demonstrate the phase behavior of these small clusters ranging from single fluid-like phase at $\Pi = 139.76$, phase coexistence at $\Pi^* = 147.74$ and single solid-like phase at $\Pi^* = 173.03$.

The outcome of weighting the configurations obtained via umbrella sampling using the FEL is shown as an OP phase space plot in Fig. 2.8. Fig. 2.8(c) is the master data set comprising data points in both fluid-like and solid-like basins of the underlying original FEL. Figs. 2.8(a) and 2.8(b) are the subsets of the master data set that contain only the fluid-like and solid-like data points respectively. Each of the data sets in Fig. 2.8 are subjected to a DMap study.

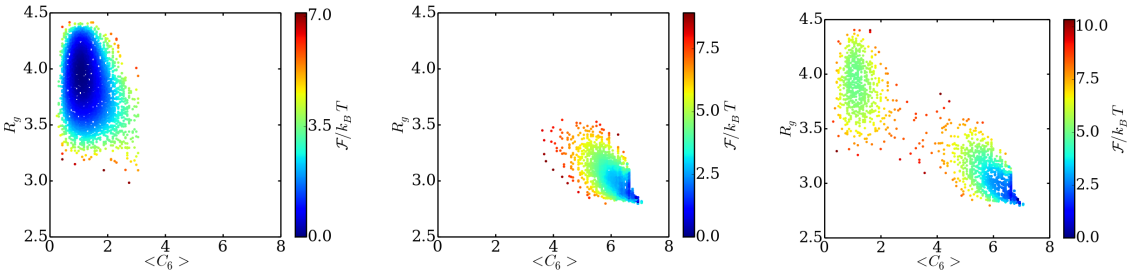


(a) Fluid well data set (b) Solid well data set. (c) Two well data set.

Figure 2.8: Data sets in $R_g - \langle C_6 \rangle$ space at $\Pi^* = 147.74$. Two well data is the master set and both fluid well and solid well are subsets of the master data set.

### 2.4.3 Eigenvalue Spectum

Fig. 2.9 shows the eigenvalue spectrum for the fluid well, crystalline well, and two-well (master) data set, respectively. A spectral gap is observed after the first non-trivial eigenvalue in Fig. 2.9(a) and the first two non-trivial eigenvalues in Figs. 2.9(b) and 2.9(c), which indicates a dimensionality of at most two.

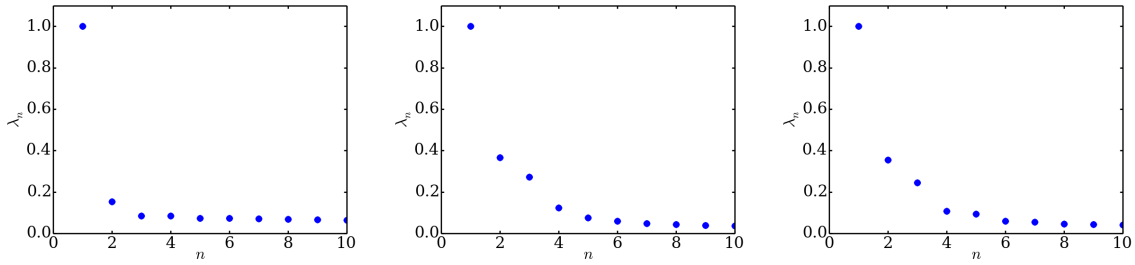


(a) Eigenvalue spectrum for fluid data.

(b) Eigenvalue for solid well data.

(c) Eigenvalue for two well data.

Figure 2.9: Eigenvalue spectra for the three data sets generated using the bootstrapped approach. The three spectra indicate a dimensionality requirement of at most two to model the assembly process.

### 2.4.4 Eigenvector Correlations & Analysis

Figs. 2.10, 2.11, and 2.12 show the data sets plotted in the coordinates of the first two non-trivial eigenvectors, i.e., in $\nu_2 - \nu_3$ space. The data points are colored by the value of order parameter $R_g^*$ in Figs. 2.10(a), 2.11(a), and 2.12(a), $\langle C_6 \rangle$ in Figs. 2.10(b), 2.11(b), and 2.12(b), and $D_{cc}^*$ in Figs. 2.10(c), 2.11(c), and 2.12(c). Fig. 2.10 shows the data for the fluid well. The DMap coordinate $\nu_2$ corresponding to the single non-trivial eigenvalue in Fig. 2.9(a), correlates best with $R_g^*$. Fig. 2.11 shows the data for the solid well. The data points are clustered both by $R_g^*$ and $\langle C_6 \rangle$, but $D_{cc}^*$ shows an excellent correlation with $\nu_2$ as indicated by the continuous change of color from left to right in Fig. 2.11(c). The two-well (master) data set is shown in Fig. 2.12. By comparing the two-well data to the solid well data in Fig. 2.11, we see that the fluid data are localized near the vertex of the angle formed by the two branches

of the crystalline data. As with the crystalline well data, $D_{cc}$ correlates best with $\nu_2$. For the data sets that include the crystalline well, Figs. 2.11 and 2.12, we observe a symmetry about the $\nu_3 = 0$ axis. This symmetry suggests that this coordinate is capturing some inversion degrees of freedom, which are not of particular interest in this study. Overall, the DMap analysis leads us to the conclusion that the OP space $\psi = \left(R_g^*, D_{cc}\right)$ will provide a better coarse-grained representation than the originally chosen space $\left(R_g^*, \langle C_6 \rangle\right)$. $R_g^*$ correlates best with the only important coordinate in the fluid well. $D_{cc}^*$ correlates best with the first important coordinate in the crystalline well, while the second important coordinate in this well seems to be associated with an inversion symmetry that is not of interest. Figs. 2.11(a), 2.11(b), 2.12(a), and 2.12(b) indicate redundancy of information contained by $R_g^*$ and $\langle C_6 \rangle$, suggesting that the latter variable may be replaced.

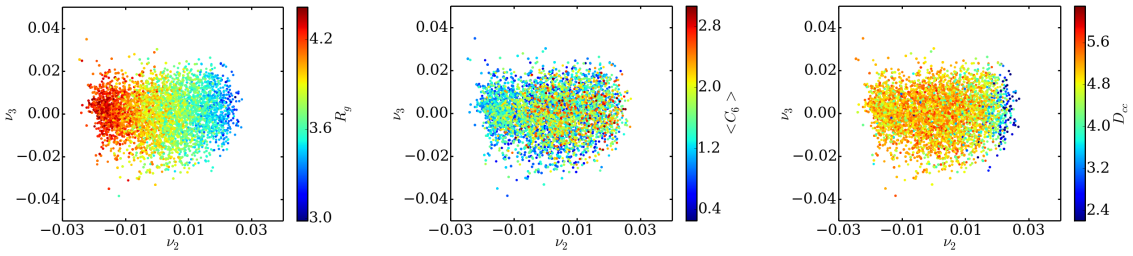


(a) Fluid data set in $\nu_2 - \nu_3$ space colored by $R_g^*$.

(b) Fluid data set in $\nu_2 - \nu_3$ space colored by $< C_6 >$.

(c) Fluid data set in $\nu_2 - \nu_3$ space colored by $D_{cc}^*$.

Figure 2.10: Eigenvector correlations for the fluid data set with the three order parameters $R_g^*, \langle C_6 \rangle$, and $D_{cc}^*$. $R_g^*$ shows the best correlation with $\nu_2$ compared to either $\langle C_6 \rangle$ or $D_{cc}^*$.

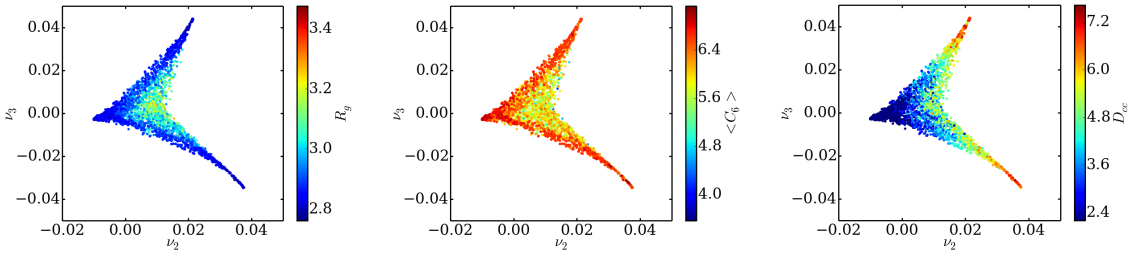


(a) Solid data set in $\nu_2 - \nu_3$ space colored by $R_g^*$.

(b) Solid data set in $\nu_2 - \nu_3$ space colored by $\langle C_6 \rangle$.

(c) Solid data set in $\nu_2 - \nu_3$ space colored by $D_{cc}^*$.

Figure 2.11: Eigenvector correlations for the solid data set with the three order parameters $R_g^*, \langle C_6 \rangle$, and $D_{cc}^*$. While $R_g^*$ and $\langle C_6 \rangle$ cluster data points, $D_{cc}^*$ shows the best correlation with $\nu_2$.

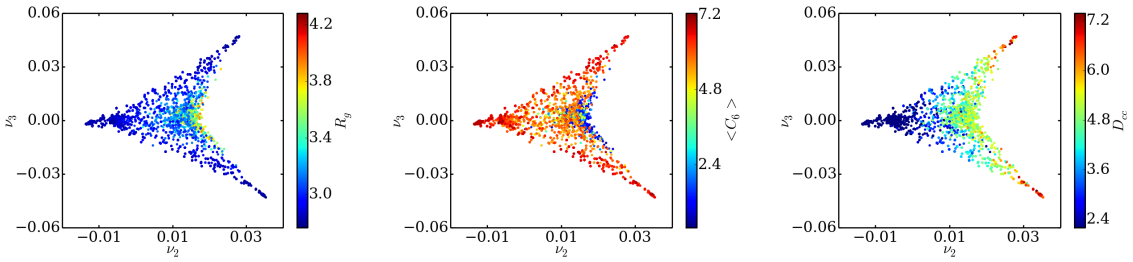


(a) Two well data set in $\nu_2 - \nu_3$ space colored by $R_g^*$.

(b) Two well data set in $\nu_2 - \nu_3$ space colored by $\langle C_6 \rangle$.

(c) Two well data set in $\nu_2 - \nu_3$ space colored by $D_{cc}^*$.

Figure 2.12: Eigenvector correlations for the two well data set with the three order parameters $R_g^*, \langle C_6 \rangle$, and $D_{cc}^*$. $R_g^*$ and $D_{cc}^*$ once again cluster data points whereas $D_{cc}^*$ shows best correlation with $\nu_2$. $\nu_3$ is a symmetry variable not important for the dynamics of this process.

We now have identified a set of OPs that correlate very well with the DMap coordinates of the data set, which we did not have before when studying a single data set from BD simulations. The bootstrapped approach helped generate data sets with complete coverage of phase space and analyze multiple data sets with diffusion maps. We discuss the low-dimensional Smoluchowski models built in $\left(R_g^*, D_{cc}^*\right)$ space in the following section.

## 2.5 Equilibrium and Dynamic Landscape Models

### 2.5.1 Free Energy & Diffusivity Landscapes

By fitting trajectories in the newly chosen coarse variable space $\psi = \left(R_g^*, D_{cc}^*\right)$ based on DMap analysis, both free energy and diffusivity landscapes are generated for four values of osmotic pressures. The reason for including a higher osmotic pressure would be explained in further detail in the following section on model validation. The FELs shown in Fig. 2.13 provides thermodynamic information on the likelihood of the system being in different regions of the OP space. The free energy differences capture the thermodynamic driving force that influences trajectory drift between different states. In the FEL in Fig. 2.13(a), there is a global minimum located around (4.9, 4.2), which corresponds to fluid-like structures. As $\Pi^*$ increases to 147.74, there is emergence of two wells located at (4.9, 3.8) and (4.1, 3.1) in Fig. 2.13(b) that indicates coexistence of fluid-like structures and solid-like structures. At higher $\Pi^*$, large free energy gradients drive fluid-like structures towards solid-like structures with low $D_{cc}^*$ and low $R_g^*$. At regions around (3.5, 3.1) in Fig. 2.13(c), there exist a local minimum with $k_BT$ scale energy barrier prior to assembly trajectories entering the global minimum near (2.2, 3.0). Fig. 2.13(d) contains a deep free energy minimum at $D_{cc}^* = 2.2$ corresponding to a single compact cluster at high attraction strengths.

The diffusivity landscapes shown in Fig. 2.14 characterize the drift and diffusion mediated by the free energy gradient. The off-diagonal terms of the diffusivity tensor $\mathbf{D}$ are negligible and not reported here. The $D_{cc}^* D_{cc}^*$ and $R_g^* R_g^*$ components are shown in figures 2.14(a)-(d) and 2.14(e)-(f) respectively. For each $\Pi^*$, the $D_{cc}^* D_{cc}^*$ component shows higher values at $D_{cc}^* \sim 2.2 - 3$, which characterize the large fluctuations due to particles attaching to or breaking from a cluster. For the $R_g^* R_g^*$ component, higher values appear at moderate extent of condensation ($R_g^* \sim 3.2 - 4.0$), where particle arrangement results in strong fluctuations in $R_g^*$. Both the diagonal components $D_{cc}^* D_{cc}^*$ and $R_g^* R_g^*$ show a decrease in magnitude at lower $R_g^*$ values as the configurations be-

come more condensed and compact allowing little room for particles to move around in the cluster, especially at increased attraction levels.

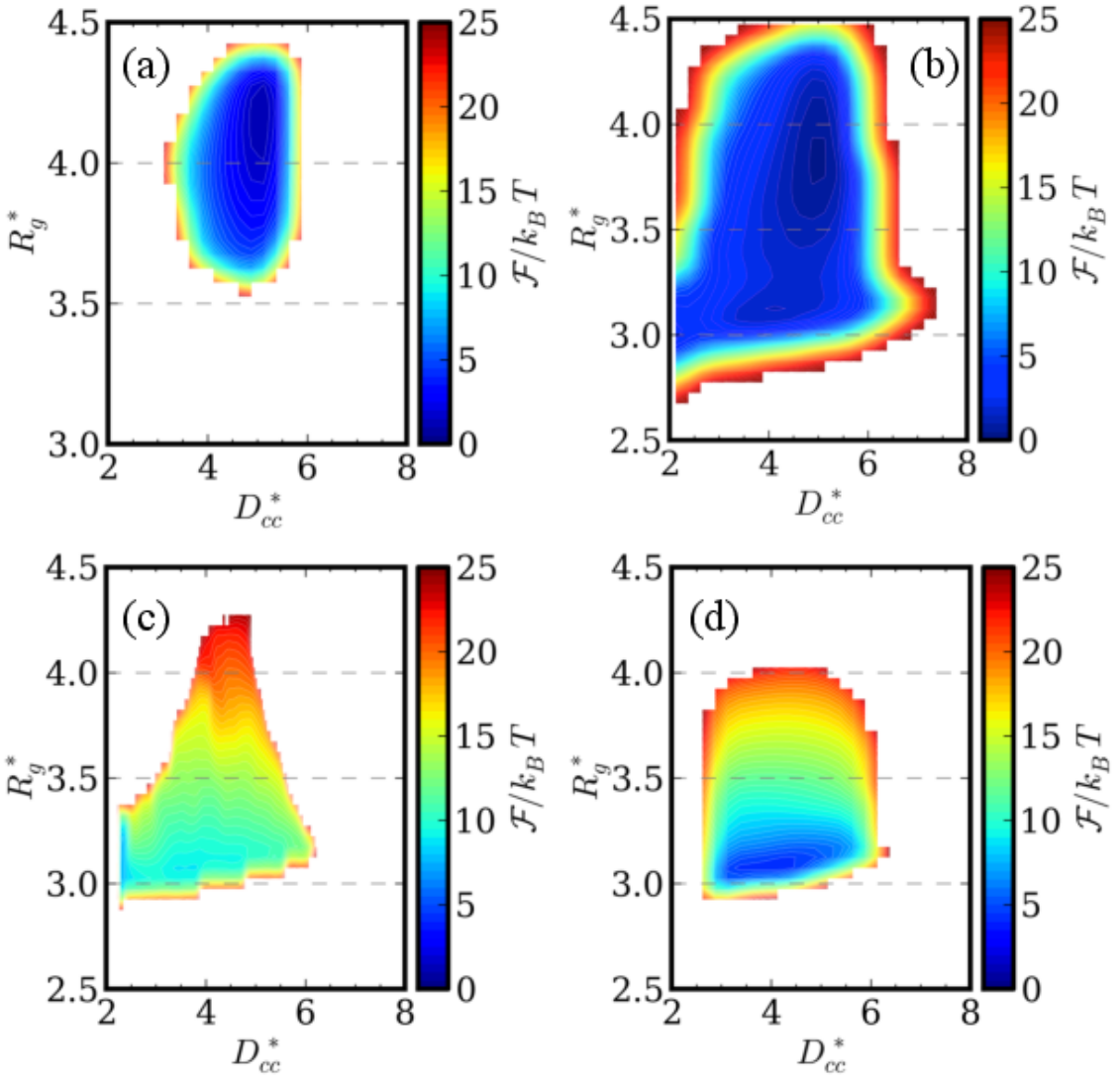


Figure 2.13: Free energy landscapes generated at four different osmotic pressures (a) $\Pi^* = 139.76$, (b) $\Pi^* = 147.74$, (c) $\Pi^* = 173.03$, (d) $\Pi^* = 252.89$ from Smoluchowski analysis.

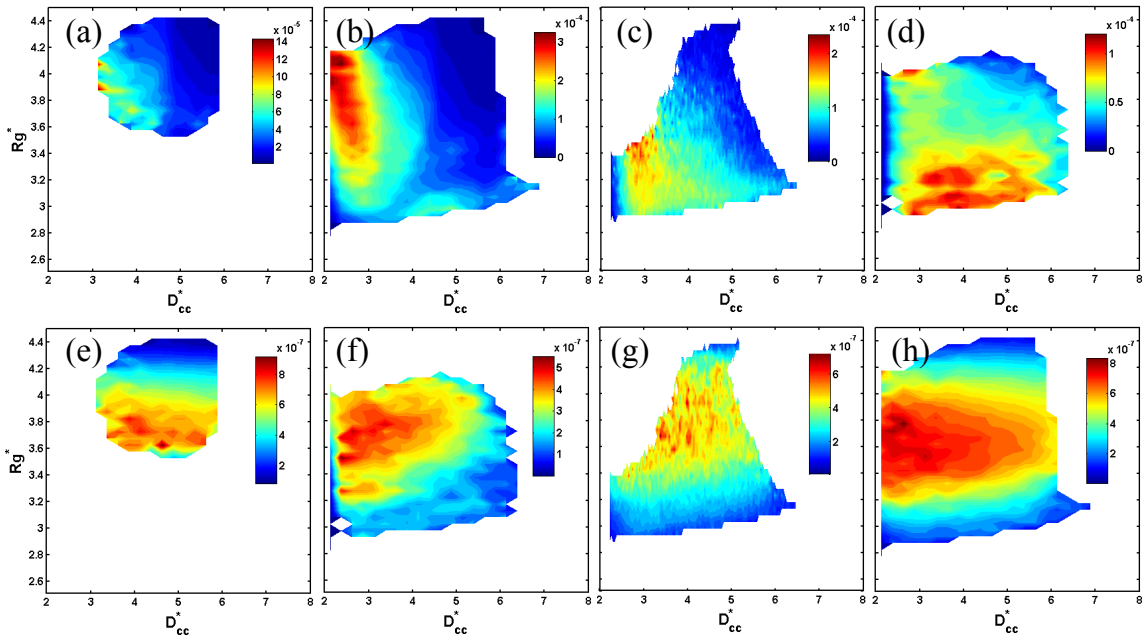


Figure 2.14: Diffusivity landscapes generated at four different osmotic pressures (a)-(e) $\Pi^* = 139.76$, (b)-(f) $\Pi^* = 147.74$, (c)-(g) $\Pi^* = 173.03$, (d)-(f) $\Pi^* = 252.89$ from Smoluchowski analysis. Top rows show the $D_{D^*_{cc}D^*_{cc}}$ component and the bottom rows show the $D_{R^*_gR^*_g}$ component.

### 2.5.2 Model Validation

The low-dimensional Smoluchowski models are examined by comparing the probability propagator constructed from particle-scale Brownian dynamic (BD) simulations and order-parameter-scale low dimensional Langevin dynamics (LDLD) simulations. The LDLD simulations are based on a Langevin equation given by [52],

$$\mathbf{\Psi}(t+\Delta t) = \mathbf{\Psi}(t) - \mathbf{D}(\mathbf{\Psi}).(k_BT)^{-1} \bigtriangledown W(\mathbf{\Psi})\Delta t + \bigtriangledown.\mathbf{D}(\mathbf{\Psi}) + [2\mathbf{D}(\mathbf{X}\Delta t)]^{1/2}\,\Gamma(t) \quad (2.12)$$

where all the symbols retain the same meaning as explained in Eq. 1.2 and $\Gamma(t)$ is a Gaussian noise term. An accurate Smoluchowski model will reproduce $\rho(\mathbf{\Psi}, t)$ obtained from high-dimensional BD simulations. Fig. 2.15 shows the comparison between BD and LDLD simulations performed at $\Pi^* = 147.74$ for an observation time $t = 10$ s for two starting points. The time scale is smaller than the global

relaxation time (i.e., order $10^3$ s) and larger than the Brownian time scale (i.e., order $10^{-1}$ s) and is expected to capture the transient assembly dynamics. Fig. 2.15 shows good agreement between BD and LDLD simulations starting at (5.2, 4.4) and (4.5, 3.2), which are the located inside the two wells at $\Pi^* = 147.74$. Similar comparisons for the fluid well at lower $\Pi^*$ and solid well at higher $\Pi^*$ confirm that the high-dimensional particle scale model can be well approximated by low-dimensional order parameter based dynamic models.

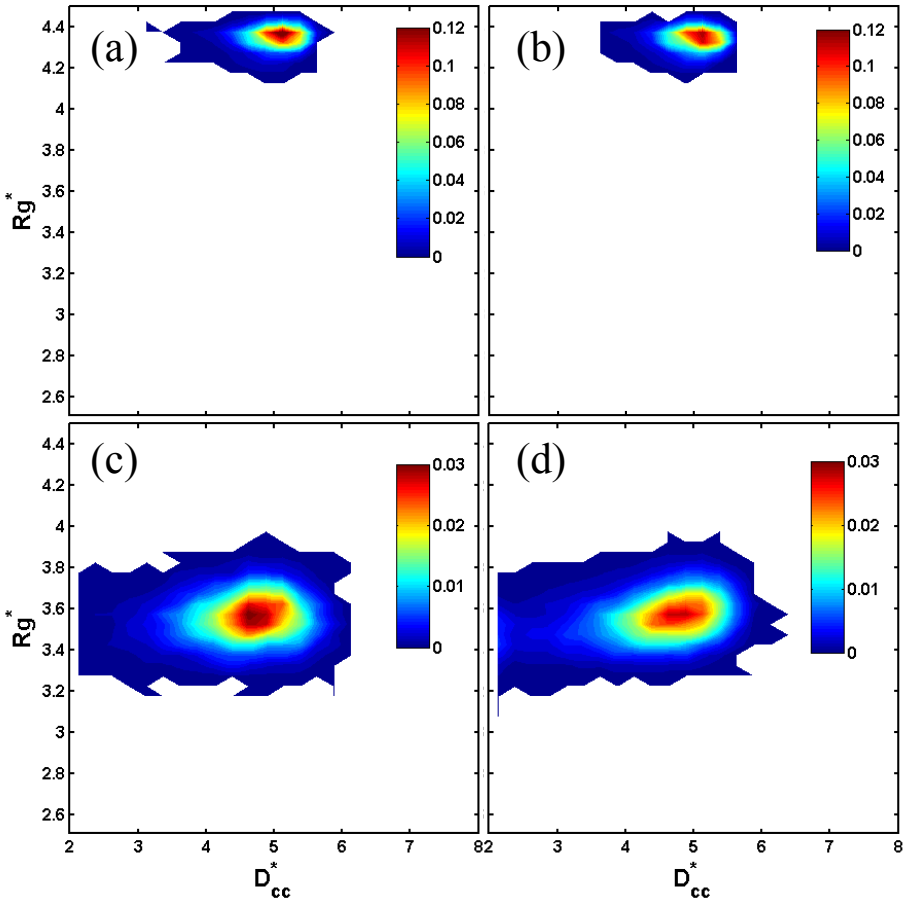


Figure 2.15: Probability propogator obtained from BD and LDLD simulations at $\Pi^* = 147.74$. Simulations were initiated from (5.2, 4.4) for (a)BD, (b)LDLD and (4.5, 3.2) for (c)BD, (d)LDLD.

## 2.6 Markov State Model for Control Policy Maps

In order to utilize the low-dimensional model for controlling the assembly, our collaborators in consultation with our group constructed a Markov decision process (MDP). MDP has previously been used to achieve a highly ordered colloidal crystal in a Markov chain transition state model of the assembly process, using electric field and depletion force as control input. Here we construct a Markov decision process framework to study the control of the colloidal crystals to form a single crystalline state using the system osmotic pressure as the control variable, and implementing the control in a BD simulation. The methods for constructing a MDP is outlined in [52]. We summarize the results below.

The first step is the validation of the model by comparing the sampling of Markov chain Monte Carlo simulations with BD simulations. Fig. 2.16 compares the Markov chain Monte Carlo simulation (1000-realization averaged) to 1000-realization averaged BD simulation. These simulations are run at constant $\Pi^*$ without control. In Fig. 2.16, 'BDUnCon' denotes the uncontrolled BD simulation and 'MCUnCon' denotes the uncontrolled Markov chain Monte Carlo simulation. All the simulations started from the same fluid-like initial state and were simulated for 500 s. The comparison shows that the transition matrices are able to approximate the BD simulation qualitatively and with reasonable quantitative accuracy, capturing the differences across the four osmotic pressure levels. Under the high $\Pi^*$ values ($\Pi_3^*$ and $\Pi_4^*$), the system is able to reach a more crystalline final state (given the same amount of simulation time), indicated by low $R_g^*$ and $D_{cc}^*$ values. Under the action of $\Pi_3^*$, system can achieve a greater degree of condenstation (low $R_g^*$), while with $\Pi_4^*$, the system gets to lower values of $D_{cc}^*$ relative to $\Pi_3^*$. It is due to this reason that we have included the fourth level of osmotic pressure ($\Pi_4^*$) and built the landscapes for all four $\Pi^*$ as discussed in the previous section. Given these observation, some combination of both $\Pi_3^*$ and $\Pi_4^*$ can lead to the desired target state.

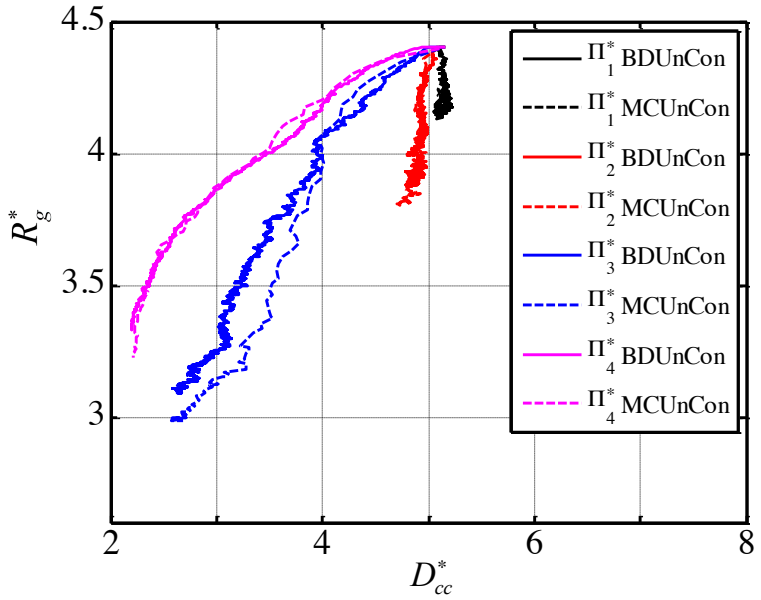


Figure 2.16: OP phase space trajectory comparison between Markov chain models and the full scale BD simulations at four $\Pi^*$ values. The Markov models are able to reasonably capture the trend at all the osmotic pressure strengths.

Given the transition matrix models, we constructed a time-independent optimal control policy with dynamic programming using the policy iteration algorithm. The objective function or the reward fucntion $R$ being minimized is given by [52],

$$R = \frac{1}{R_g^{*2}} + \frac{1}{D_{cc}^{*2}} \tag{2.13}$$

This reward function attempts to drive the system simultaneously towards low $R_g^*$ and low $D_{cc}^*$ values where free energy minimum is located at high attraction strengths. The control policy is shown in Fig. 2.17 as a lookup table. The numbers in the color bar stand for the control action $\Pi^*$ values, increasing from $\Pi_1^*$ to $\Pi_4^*$ accordingly. Given its time-independent property, with the current $R_g^*$ and $D_{cc}^*$ values known, the corresponding control action can be taken directly from this table. With approximately 10,000 discrete states, the policy calculation can be achieved in only a few minutes.

According to Fig. 2.17, the optimal control policy is mostly confined to the use of the high $\Pi^*$ values, $\Pi_3^*$ and $\Pi_4^*$. When the system is close to the global minimum point around $R_g^* = 2.8$ and $D_{cc}^* = 2.2$, $\Pi_4^*$ is used to lock the system in the minimum. A single controlled BD simulation is plotted on top of the policy map, starting from a fluid-like state of $R_g^* = 3.78$, $D_{cc}^* = 5.0$. A combination of $\Pi_3^*$ and $\Pi_4^*$ is able to drive the system close to the global free energy minimum.

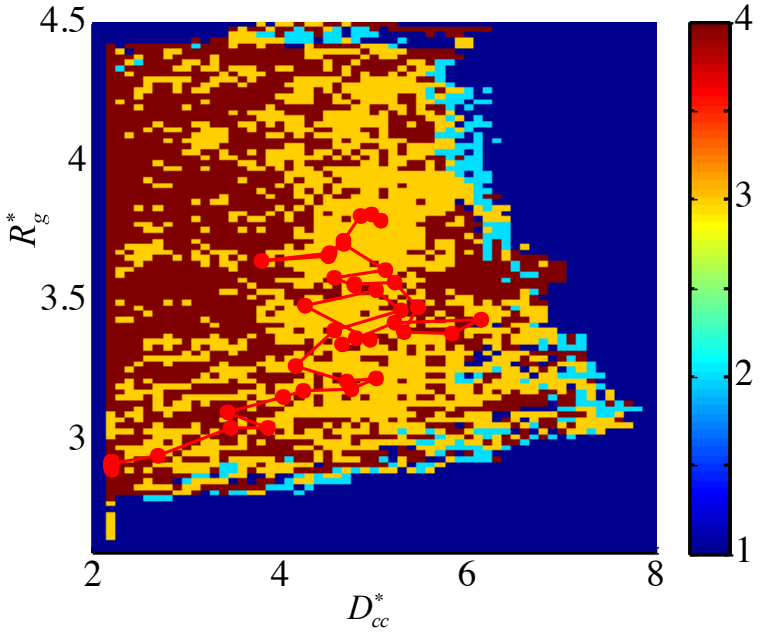


Figure 2.17: Optimal control policy for four osmotic pressures computed from Markov chain model using dynamic programming. A combination of $\Pi_3^*$ and $\Pi_4^*$ drive the system from a fluid-like state to the global free energy minimum as shown by the red trajectory.

The effectiveness of the control policy is evaluated by applying it to both the Markov chain model as well as BD simulations. A comparison of 250-realization-averaged order parameter simulation results with and without control in BD simulations is shown in Fig. 2.18. In Fig. 2.18, the trajectory labeled 'BDCon' stands for 250-realization-averaged BD simulations with control. Trajectories labeled 'BD$\Pi^*$' are 250-realization-averaged BD simulations under constant $\Pi^*$ values. All these trajectories are simulated for 500 s, starting from the same initial fluid-like state of

$R_g^* = 3.78$ and $D_{cc}^* = 5.0$. Fig. 2.18(a) shows the average trajectories in the OP phase space. Inspection of the controlled trajectory reveals a decrease in the final $D_{cc}^*$ value, compared to that under the action of $\Pi_3^*$, as well as a lower $R_g^*$ value compared to that under the action of $\Pi_4^*$. Fig. 2.18(b) shows the same trajectory as a function of time. In all three cases, the time scales for the system response are similar, but end up at different terminal states.

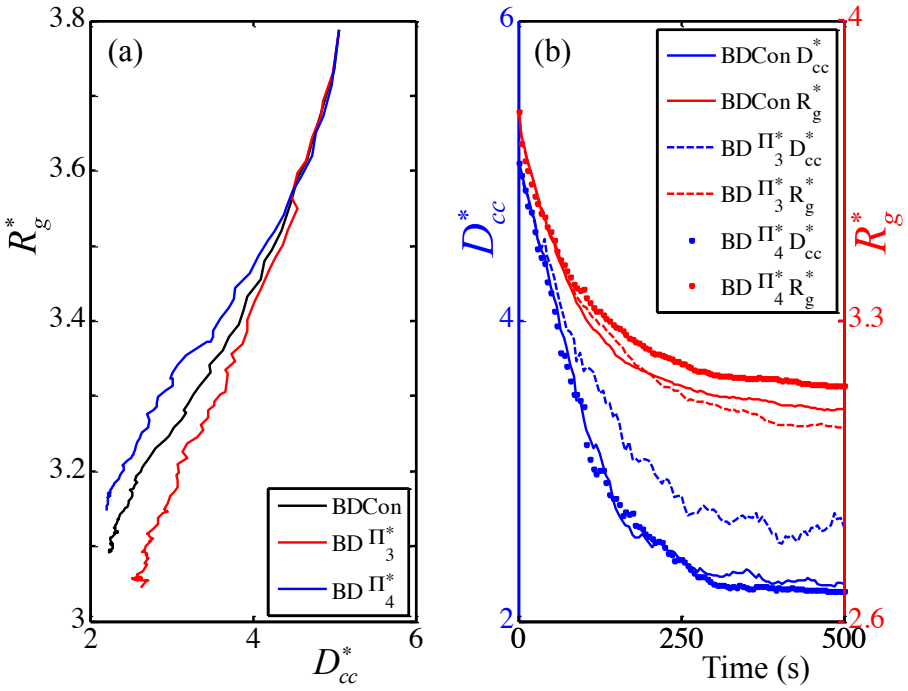


Figure 2.18: Comparison between 500 s long, 250 realization-averaged order parameter trajectories with and without control policy.

## 2.7 Summary & Conclusions

We studied the phase behavior of a small cluster of silica colloidal particles in aqueous solution interacting via a temperature tunable $k_BT$ scale depletion potential. We modeled the thermodynamic and dynamic behavior by building a low-dimensional Smoluchowski model in a coarse-grained order parameter phase space. We applied a bootstrapped diffusion mapping technique to determine suitable order parameters

to build the low-dimensional models. The initial coarse variable pair $(R_g, \langle C_6 \rangle)$ was chosen from a previously existing model where the diffusion maps did not show any significant correlations with either $R_g^*$ or $\langle C_6 \rangle$. We introduced a third order parameter, average cluster to cluster distance metric, $D_{cc}^*$, that was able to track the breakage or coalescence of clusters in the assembly. By use of the bootstrapped technique, we were able to generate mutliple data sets that spanned the fluid-like and solid-like regions of phase space and studied the correlations of the candidate order parameter set with the non-trivial eigenvectors. $R_g^*$ showed excellent correlation with the eigenvector in the fluid data set while $D_{cc}^*$ showed excellent correlation with the eigenvector in data sets that included the solid-like well. We replaced $\langle C_6 \rangle$ with $D_{cc}^*$ and built energy and diffusivity landscapes in $\left(R_g^*, D_{cc}^*\right)$. The Smoluchowski models were validated by comparison of full scale BD simulations with low dimensional Langenvin dynamic simulations in the coarse variable space. Markov state models were also built for computing a control policy sequence that utilized the information from the landscape models to optimally guide the system towards the desired target crystal structure.

# CHAPTER 3

# COARSE-GRAINED LANDSCAPE MODELS: ELECTRIC FIELD (QUADRUPOLE) SYSTEM

## 3.1 Introduction

The second model system we investigate is the electric field mediated assembly or the quadrupole system. It comprises an assembly of colloidal silica particles $\sim 3$ $\mu$m in diameter confined within quadrupole electrodes that are connected to a generator. The high frequency AC applied electric field causes the formation of induced dipoles in the colloids. These induced dipoles interact with the electric field and with each other. Fig. 3.1(a) and Fig. 3.1(b) show the co-planar thin gold film quadrupole electrode. Fig. 3.1(c) shows the cluster of colloids in the center of the electrodes and Fig. 3.1(d) is the contour plot of the electric field and the field strength is minimum at the center of the electrodes. The interaction energy between the colloids is modeled as a combination of electrostatic double layer (DLVO), induced dipole-inhomogeneous electric field, and induced dipole-induced dipole interactions [16–20]. The gravitational potential acts in the direction normal to the underlying wall and helps confine colloids to a monolayer. The net potential energy for the system is given by,

$$u_{\text{net}}(\mathbf{r}) = \sum_{i=1}^{N} u_{de,i}^{pf} + \sum_{\langle i,j \rangle} \left( u_{e,i,j}^{pp}(\mathbf{r}) + u_{dd,i,j}^{pp}(\mathbf{r}) \right) \tag{3.1}$$

where $\mathbf{r}$ is the 3N dimensional vector with position information of all particles in the system, $u_{e,i,j}^{pp}(\mathbf{r})$ is the electrostatic potential between particles $i$ and $j$, and $u_{dd,i,j}^{pp}(\mathbf{r})$ is the induced-dipole induced-dipole potential between particles $i$ and $j$, and $u_{de,i}^{pp}(\mathbf{r})$ is the induced dipole-inhomogeneous electric field potential of particle $i$.

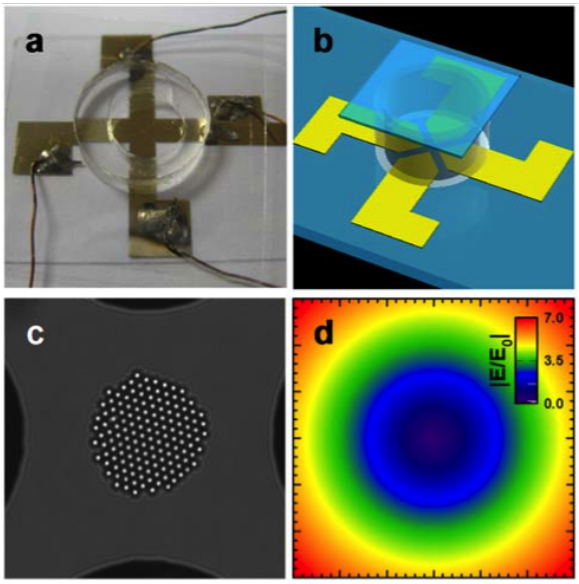


Figure 3.1: Co-planar thin gold film quadrupole electrode. (a) Top view of device showing connections to the generator. (b) Schematic of the device setup. (c) 3 $\mu$m silica colloids in the quadrupole electrode center at the electric field minimum. (d) Contour plot of the electric field with linear spectrum scale [19, 20].

An interesting feature of this system is the formation of different microstructures like fluids, quasi-2D chains, polycrystalline configurations with multiple misoriented domains, and hexagonal packed crystals. In particular, polycrystalline configurations form due to coalescence of individual crystal domains at increased field strength resulting in grain boundaries and the migration of the defects towards edge of the crystal results in formation of nearly perfect crystal structures [53]. In contrast, we noticed a phase change from a fluid-like to a crystalline configuration in the case of depletion potential in Chapter 2. Here we seek to probe this feature of grain boundary formation and annealing of defective microstructures to form perfect crystals by use of the diffusion mapping technique.

## 3.2 Diffusion Mapping Analysis: Dimensionality & Order Parameters

### 3.2.1 Order Parameters

We have used three order parameters to characterize the particle configurations in this system. The first metric is radius of gyration, $R_g$ which is used to capture the condensation of the clusters. It is calculated as given in the equation

$$R_g = \left( \frac{1}{N} \left[ \frac{1}{2} \sum_{i,j} |\mathbf{r}_i - \mathbf{r}_j|^2 \right]^{0.5} \right) / R_{g,\mathrm{Hex}} \tag{3.2}$$

where $a$ is the particle radius and $N$ is the system size. $R_{g,\mathrm{Hex}}$ is the normalizing factor which is the radius of gyration for 2D HCP clusters with regular polygon morphologies and is given by [54],

$$R_{g,\mathrm{Hex}} = \frac{\sqrt{5}}{3} a N^{0.5} \tag{3.3}$$

The presence of global order in the crystals is estimated using $\psi_6$ [55] calculated as

$$\psi_{6,j} = \frac{1}{N_{C,j}} \sum_{k=1}^{N_{C,j}} e^{i6\theta_{jk}} \tag{3.4}$$

$$\psi_6 = \frac{1}{N} \sum_{j=1}^{N} \psi_{6,j} \tag{3.5}$$

where $\psi_{6,j}$ is the six-fold bond orientation order parameter of particle $j$, $N_{C,j}$ is the number of neighbors with the coordination radius of particle $j$, $\theta_{jk}$ is the angle between particle $j$ and each neighboring particle with an arbitrary reference direction, and $\psi_6$ is the average local bond orientation determined by averaging over all particles, which produces values between zero and one. The third order parameter is $\langle C_6 \rangle$, which is the average local six-fold connectivity order. It is calculated from the following equations.

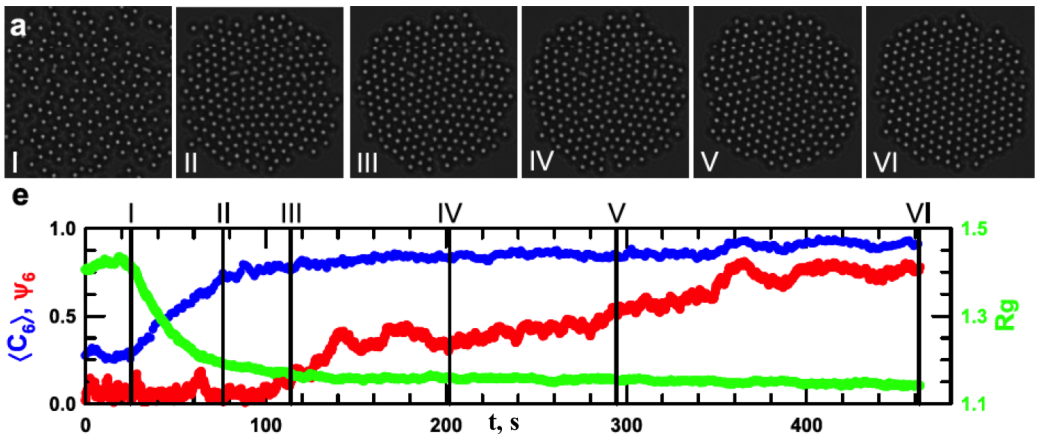


Figure 3.2: (a) Microstructure evolution of the 210 quasi-2D colloidal systems from quadrupole experiments and (e) the corresponding evolution of the three order parameters $R_g$, $\langle C_6 \rangle$, and $\psi_6$ [53].

$$\chi_{6,jk} = \frac{|Re\left[\chi_{6,j}\chi^*_{6,k}\right]|}{|\chi_{6,j}\chi^*_{6,k}|} \tag{3.6}$$

$$C_6(j) = \sum_{k=1}^{N_C(j)} \begin{bmatrix} 1 & \chi_{6,jk} \geq 0.32 \\ 0 & \chi_{6,jk} < 0.32 \end{bmatrix} \tag{3.7}$$

$$\langle C_6 \rangle = \frac{1}{N}\sum_{i=1}^{N} C_6(i) \tag{3.8}$$

Fig. 3.2 shows the various microstructures formed during the experiment. The plot also shows the evolution of the three order parameters. $R_g$ decreases instantly as a result of the condensation and $\langle C_6 \rangle$ increases as a result of emergence of local order in the crystal. However, $\psi_6$ is sensitive to the defects and it gradually increases as the grain boundaries migrate towards the edge of the crystal domain.

Fig. 3.3 shows three representative snapshots with their order parameter values. $R_g$ is able to distinguish between fluid-like configuration in Fig. 3.3(a) and condensed clusters in both Figs. 3.3(b) and 3.3(c). $\langle C_6 \rangle$ is a meaure of only local order and is high for both defective and nearly perfect clusters while $\psi_6$ is sensitive to the presence of defects and can distinguish between the two states in Figs. 3.3(b) and 3.3(c).

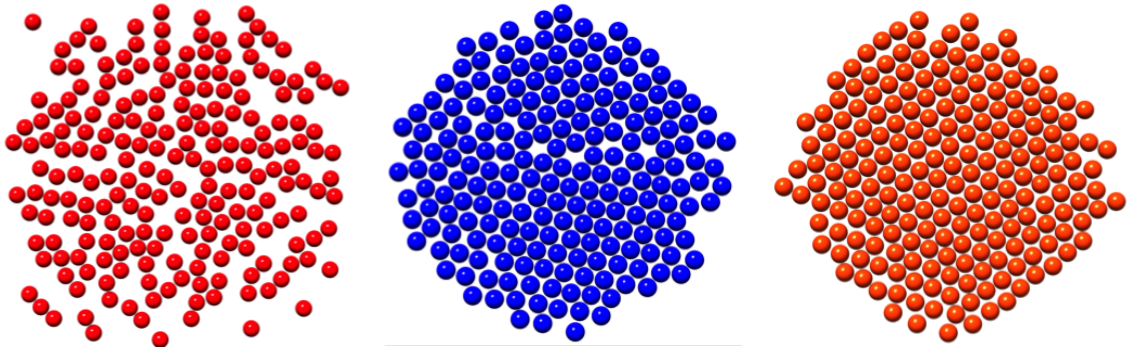

(a) $R_g = 14.7, \langle C_6 \rangle = 2.12, \psi_6 = 0.105$.

(b) $R_g = 11.75, \langle C_6 \rangle = 5.03, \psi_6 = 0.242$.

(c) $R_g = 11.58, \langle C_6 \rangle = 5.37, \psi_6 = 0.92$.

Figure 3.3: Representative configuration snapshots with their order parameter values for $R_g, \langle C_6 \rangle$, and $\psi_6$.

### 3.2.2 Data Sets

For the diffusion mapping analysis, a large number of configuration (snapshots) were generated using BD simulations for a system size of $N = 210$ with a normalized voltage $V^* = 0.80$. The data set contains $\sim 8000$ configurations spanning all relevant regions of phase that includes fluid-like, polycrystalline, and crystalline states. The data sets are shown in OP space in Fig. 3.4. We note that both $R_g$ and $\langle C_6 \rangle$ show a high degree of correlation with condensation and emergence of local order as can be seen in Fig. 3.4(b). However $\psi_6$ shows a gradual increase towards unity as the defects migrate towards the edge of the crystal. The diffusion mapping analysis for this data set follows.

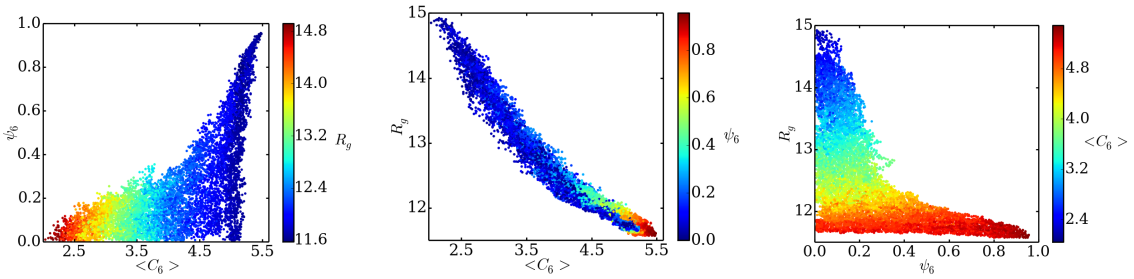


(a) BD data set in $\langle C_6 \rangle - \psi_6$ space colored by $R_g$.

(b) BD data set in $\langle C_6 \rangle - R_g$ space colored by $\psi_6$.

(c) BD data set in $\psi_6 - R_g$ space colored by $\langle C_6 \rangle$.

Figure 3.4: BD data sets for field assembly plotted in the space of $R_g, \langle C_6 \rangle$, and $\psi_6$. The set contains fluid-like, polycrystalline and perfect crystalline configurations.

### 3.2.3 Eigenvalue Spectum

The eigenvalue spectrum from diffusion maps exhibits a large spectral gap after $\lambda_2$ and a smaller gap after $\lambda_4$, as shown in Fig. 3.5. This spectrum indicates a strong one-dimensional characteristic to the data, with the possibility of two additional dimensions of lesser importance.

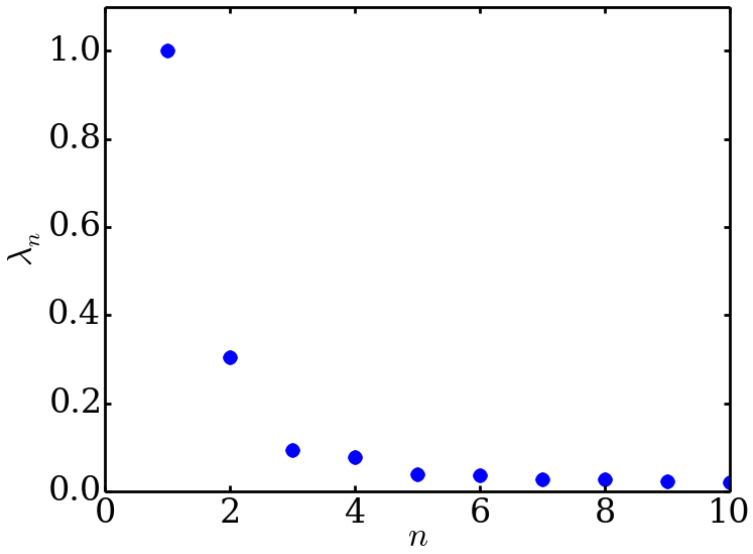


Figure 3.5: Eigenvalue spectrum for the BD dataset contains a big spectral gap after the first non-trivial eigenvalue $\lambda_2$ and a smaller gap after the third non-trivial eigenvalue $\lambda_4$. This implies a strong one-characteristic to the data, with two additional dimensions of lesser importance.

### 3.2.4 Eigenvector Correlations & Analysis

The data are plotted in the space of corresponding non-trivial eigenvectors, $\nu_2 - \nu_3$ space in Fig. 3.6 and $\nu_2 - \nu_4$ space in Fig. 3.7. We observe that the data are clustered into two distinct one-dimensional objects that are mirror images across the $\nu_4 = 0$ axis in Fig. 3.7. Therefore we conclude that $\nu_4$ is likely a symmetry variable of no importance to the intrinsic dynamics of the assembly process. Projection of the data onto the $\nu_2 - \nu_3$ space in Fig. 3.6 suggests that the points lie on a one-dimensional curve, implying that $\nu_3$ has a functional dependence on $\nu_2$. Ferguson *et al.* [45] reported that such functional dependencies indicate multiple eigenvectors characterizing the same dynamic pathway. Although not shown in the figures here, we have also plotted the data in the coordinate space of higher-order eigenvectors, up to $\nu_8$, and the data always appear to remain on a one-dimensional manifold.

We also studied how the eigenvectors correlate with the candidate order parameters that have been described previously by coloring plots in Figs. 3.6 and 3.7. Fig. 3.6(a) shows that $R_g$ is very well correlated with $\nu_2$, as indicated by the continuous spectrum of color in the $\nu_2$ coordinate. Fig. 3.6(c) shows that data points with larger values of $\psi_6$ are clearly confined to the region of high $\nu_2$ values, and while there is some clustering of points by color in that region, $\psi_6$ does not show a significant correlation with any of the top three eigenvectors. From the diffusion mapping analysis, we conclude that the data lie on a one-dimensional manifold that is strongly correlated with $R_g$ but not with $\psi_6$.

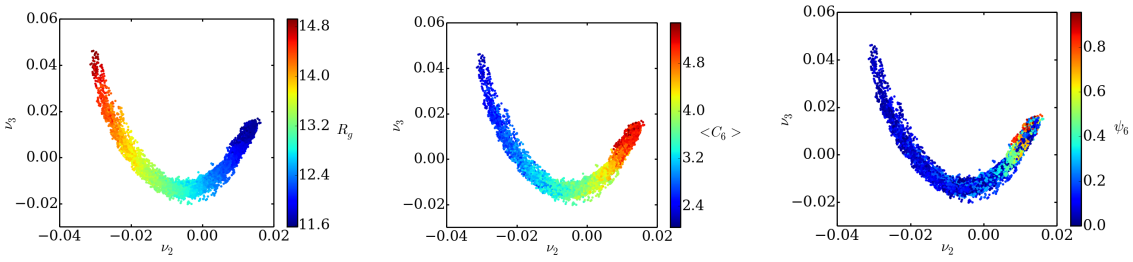


(a) Data in $\nu_2 - \nu_3$ space colored by $R_g$.

(b) Data in $\nu_2 - \nu_3$ space colored by $\langle C_6 \rangle$.

(c) Data in $\nu_2 - \nu_3$ space colored by $\langle C_6 \rangle$.

Figure 3.6: Data set plotted in $\nu_2 - \nu_3$ space colored with the OPs $R_g, \langle C_6 \rangle$, and $\psi_6$. Date points lie on a one dimensional curve with $\nu_3$ being a strong function of $\nu_2$. $R_g$ shows the best correlation with $\nu_2$.

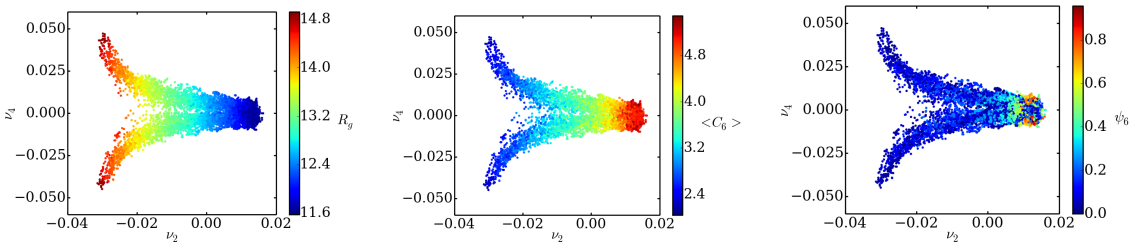


(a) Data in $\nu_2 - \nu_4$ space colored by $R_g$.

(b) Data in $\nu_2 - \nu_4$ space colored by $\langle C_6 \rangle$.

(c) Data in $\nu_2 - \nu_4$ space colored by $\psi_6$.

Figure 3.7: Data set plotted in $\nu_2 - \nu_4$ space colored with the OPs $R_g, \langle C_6 \rangle$, and $\psi_6$. $\nu_4$ is a symmetry variable that is not important to the dynamics of the process.

### 3.2.5 Limitations of the Hausdorff Distance Metric

We examined the sensitivity of the Hausdorff distance metric that was used in the construction of the probability transition matrix **M**. We isolated snapshots in phase space that represent fluid-like, defective crystals and perfect crystal states and randomly chose snapshots from each state that were not correlated in BD time or MC trajectory but had similar order parameter values $R_g$ and $\psi_6$. The average Hausdorff distance metric between expanded and condensed states was much higher than those between defective and perfectly ordered crystals. Thus the distinction

between defective and perfect crystals is not sharp in the distance metric. This is best observed in Fig. 3.8 which shows the blurred boundary between defective and perfect crystals. This analysis also reveals why condenstaion and not grain boundary motion is the only dominant feature of the directed assembly process as perceived by diffusion maps.

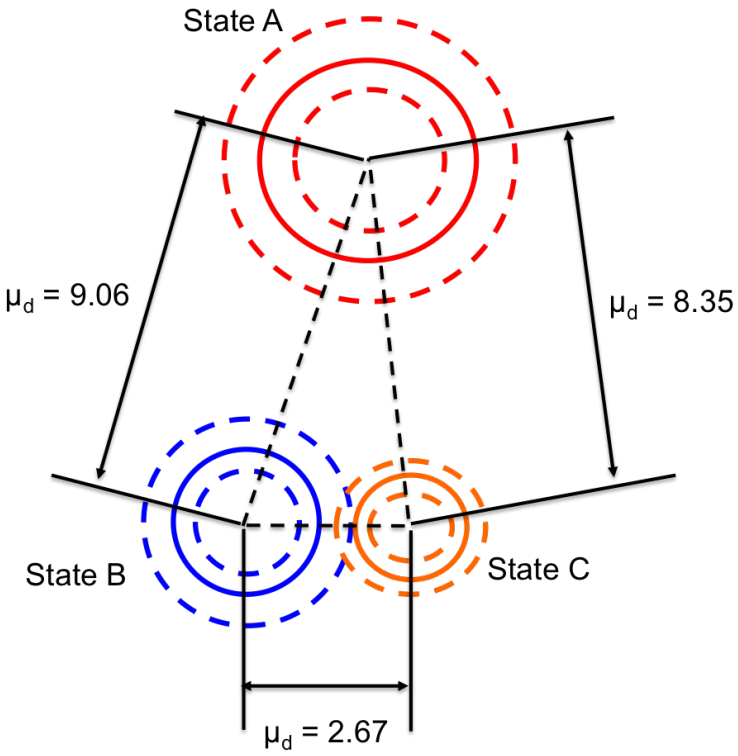


Figure 3.8: State (A) Expanded fluid-like structures State (B) Condensed defective structures and State (C) Condensed perfect crystal structures. The dashed circles around each solid circle is a measure of variations of Hausdorff distance within each state. The more interesting observation is the average distance $\mu_d$ between states A-B or A-C is much greater than B-C, i.e. $\mu_{d,AB} \sim \mu_{d,AC} \gg \mu_{d,BC}$.

### 3.2.6 Modification of the Distance Metric in DMap Analysis

Based on the limitations of Hausdorff distance metric, we modified the distance metric used in the DMap analysis by augmenting the distance metric with an angular contribution that accounts for the local orientational arrangement about each particle

in the cluster. The local orientation distance metric between snaphot $i$ and $j$, $\mathbf{O}$, is given by [56],

$$O_{ij} = \min_{\theta_t} \parallel h_i(\theta) - h_j(\theta + \theta_t) \parallel_2 \tag{3.9}$$

where $h_i(\theta)$ is the normalized bond angle histogram for snapshot $i$, $\theta_t$ is the offset in order to achieve the global optimal alignment. This orientational metric is combined with Hausdorff distance metric to effectively yield an augmented distance metric

$$\Delta_{ij} = \left[ \left( \frac{H_{ij}}{||H||_2} \right)^2 + \left( \frac{O_{ij}}{||O||_2} \right)^2 \right] \tag{3.10}$$

The diffusion mapping results (for the same data set used before) with the new distance metric are shown in Fig. 3.9. The eigenvalue spectrum in Fig. 3.9(A) is similar to Fig. 3.5 where there is a large spectral gap after the first non-trivial eigenvalue and a smaller gap after the third. The top three non-trivial eigenvectors are plotted in Figs. 3.9(C),(D) and the data points effectively lie on a two dimensional manifold. We observe from both Figs. 3.9(B),(C) that $R_g$ shows a very good correlation with $\nu_2$. We also observe from Fig. 3.9(D) that $\psi_6$ is some function of both $\nu_2$ and $\nu_3$ while $\nu_4$ has a strong functional dependence on $\nu_2$ and does not contribute towards the dynamics of the process. We should note here that the correlation (as seen by the color separation) shown by $\psi_6$ is much better than the correlation observed in Fig. 3.6(c). The new distance metric can differentiate between defective and perfect crystals and this is manifest in the improved correlations $\psi_6$ shows with the eigenvectors. Thus we conclude from this analysis that both $R_g$ and $\psi_6$ are the most suitable order parameter candidates to build the Smoluchowski model.

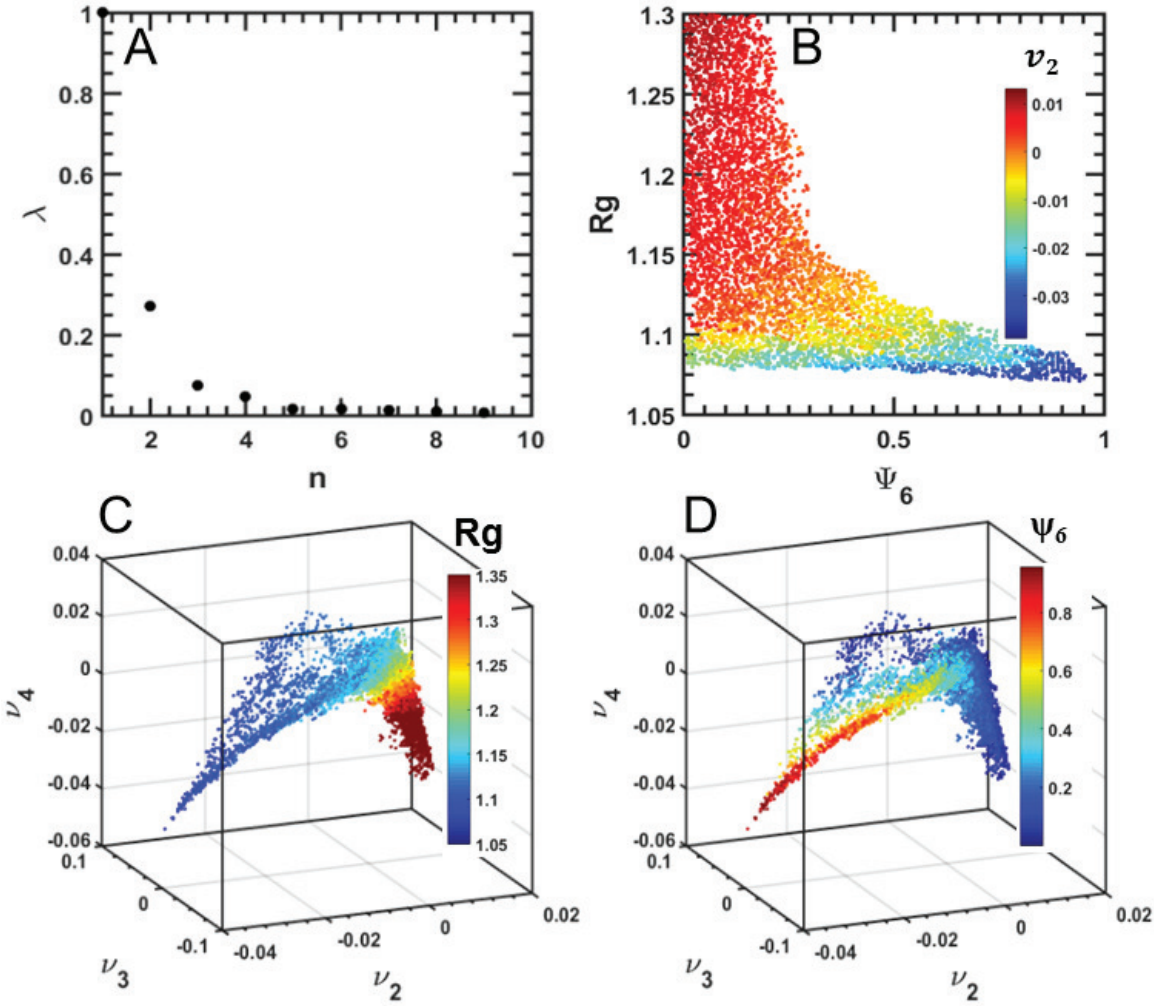


Figure 3.9: (A) Eigenvalue spectrum shows a big spectral gap after $\lambda_2$ and smaller gap after $\lambda_4$ (B)Phase space plot of $R_g - \psi_6$ colored by first non-trivial eigenvector $\nu_2$ (C) Data set in $\nu_2 - \nu_3 - \nu_4$ space shows a very good correlation between $\nu_2$ and $R_g$ (D) Data set in $\nu_2 - \nu_3 - \nu_4$ space shows that $\psi_6$ is some function of both $\nu_2$ and $\nu_3$.

## 3.3 Equilibrium & Dynamic Landscape Models

### 3.3.1 Free Energy & Diffusivity Landscapes

Based on the diffusion mapping analysis, free energy and diffusivity landscapes are constructed in the OP space $R_g$ and $\psi_6$. At the lowest voltage $V^* = 0.42$ shown in Fig. 3.10(A), the global minimum is located at $\psi_6, R_g \sim .25, 1.18$ and configurations in the vicinity of the minimum have a dense fluid-like structure consisting of several

ordererd clusters. These configurations (rendering I of Fig. 3.10(A)) lack global order due to weak electric field strength incapable of compressing the induced dipoles to form close packed structures. A single trajectory on top of the energy landscape in Fig. 3.10A shows the compression of an expanded fluid like state and its approach towards the global minimum. The four diffusivity components are shown in the middle column of Fig. 3.10(A). The $D_{\psi_6\psi_6}$ component (upperleft) has relatively large values in the neighborhood of $\psi_6 \sim 0.2-0.3$, which is consistent with grain boundary motion in polycrystalline structures that produces larger fluctuations in $\psi_6$. Cross terms in the diffusivity landscapes, both $D_{R_g\psi_6}$ and $D_{\psi_6 R_g}$ have values mostly close to zero, except for slightly negative values in the vicinity of $\psi_6, R_g \sim 0.4, 1.18$. These negative values indicate a weak coupling between the condensation and the ordering process.

As voltage is increased to $V^* = 0.5$, the global minimum shifts to $\psi_6, R_g \sim 0.6, 1.14$, showing increased condensation and global ordering as seen in Fig. 3.10(B). The equilibrium structure (rendering III) has a single central hexagonal close packed core surrounded by a thin fluid-like envelope. The free energy gradient in the $R_g$ direction is steeper at higher voltages, while it is shallow in the $\psi_6$ direction. The bi-domain crystals shown with low values of both $\psi_6$ and $R_g$ (rendering II) have misorientation angles close to 30°, which are metastable structures with minimal driving force for grain boundary migration. For the DL at this voltage, both the diagonal components decrease as $R_g$ becomes smaller, owing to the formation of dense clusters that hinders particle rearrangement. At the highest voltage $V^* = 0.57$ shown in Fig. 3.10(C), the global minimum is at $\psi_6, R_g \sim 0.6, 1.14$, with more ordered and condensed equilibrium structures (rendering VI). The free energy plateau region extends along $\psi_6 \sim 0 - 0.5$ at low $R_g$ values.

The FEL in Fig. 3.10(C) contains two typical assembly pathways denoted as T1 and T2. The T1 trajectory corresponds to rapid condensation along a steep free

energy gradient where two locally ordered domains coalesce into a bi-crystal with a near maximum 30 ° misorientation angle. From V to VI, the bi-crystal relaxes into a single domain as one grain grows at the expense of the other.

In contrast to T1, the T2 trajectory develops higher global order via initial stochastic motion before it moves down the free energy gradient and is rapidly funneled towards the global free energy minimum. The intermediate microstructure (rendering IV) is typically characterized by domains with similar orientation (i.e. small misorientation angle). Domains with small misorientation angles easily relax during coalescence and condensation, which is consistent with a smaller free energy barrier to grain boundary motion. As a result, T2 is able to bypass the free energy plateau at low $R_g$ to avoid the slow diffusion process encountered in the T1 trajectory, which results in much faster equilibration the global free energy minimum single crystal. For all voltages, all diffusivity components uniformly decreases with decreasing $R_g$, so that paths T1 and T2 do not experience significantly different levels of friction as part of determining the total time to produce single perfect crystals.

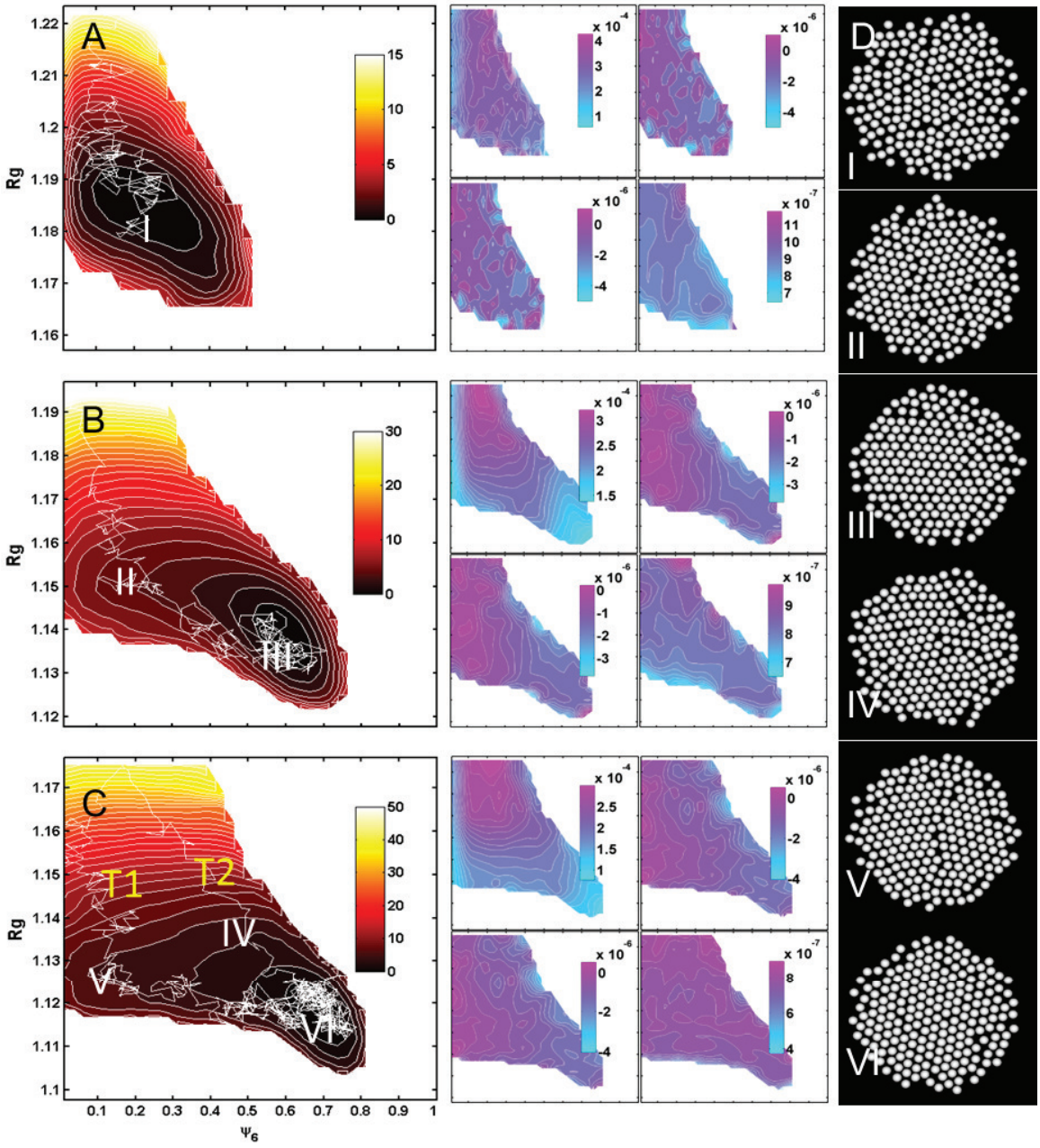


Figure 3.10: FELs and DLs from the Smoluchowski model constructed at (A) $V^* = 0.42$ (B) $V^* = 0.50$ (C) $V^* = 0.57$. Left column contains the FELs with sample trajectories plotted in the OP phase space. Middle column contains the diffusivity tensor components (left-to-right, top-to-bottom): $D_{\psi_6\psi_6}$, $D_{\psi_6 R_g}$, $D_{R_g\psi_6}$ and $D_{R_g R_g}$ Last column shows representative configurations for the coordinates marked on the FEL in the left column.

### 3.3.2 Model Validation

The low-dimensional models based on the landscapes shown in Fig. 3.10 not only provide qualitative information about the assembly process but also quantitatively capture assembly dynamics. By evaluating statistical properties of trajectories from the full N-dimensional BD simulations and low-dimensional Langevin dynamic (refer to Eq. 2.12 for the Langenvin equation) simulations, such as the first passage times for transitions from one state to another, it is possible to evaluate the accuracy of the LDLD model. Fig. 3.11 compares first passage time distributions from BD and LDLD simulations at $V^* = 0.57$. First passage time distributions show histograms of the times it takes to pass for the first time between initial states and end states characterized by $(\psi_6, R_g)$ coordinates on the FEL. The first passage time is a distribution due to the stochastic nature of the assembly dynamics.

As depicted in Fig. 3.11(A), we simplify the presentation of first passage time distributions by comparing assembly processes characterized by either (1) condensation along the steep free energy gradient parallel to the $R_g$ axis (Fig. 3.11(B)), or grain boundary relaxation along the free energy plateau parallel to the $\psi_6$ axis (Fig. 3.11(C)). For as assembly driven by condensation, Fig. 3.11(B) shows a set of first passage time distributions for assembly trajectories between initial and final $R_g$ coordinates specified in the figure caption. These distributions are obtained by averaging over all $\psi_6$ coordinates sampled during condensation. In the case of trajectories dominated by grain boundary relaxation, Fig. 3.11(C) shows first passage time distributions for trajectories between initial and final $\psi_6$ coordinates, which are averaged over all $R_g$ coordinates. It is interesting to note that the mean first passage time for grain boundary motion is an order of magnitude higher when compared to condensation. A very good agreement is observed between the $N$-dimensional BD simulations and the LDLD simulations, confirming the accuracy of the landscape models from the Smoluchowski analysis.

Fig. 3.11(D) also shows first passage time distributions roughly corresponding to trajectories T1 and T2 in Fig. 3.10(C). The fast T2 trajectory makes it to the global free energy minimum single crystal nearly two orders of magnitude faster than the slow T1 trajectory that is slowed down by the presence of the free energy plateau corresponding to grain boundary diffusion. This large difference in first passage times is not captured when projecting onto a single dimension ($R_g$ or $\psi_6$) as shown by the first passage times in Figs. 3.11(B),(C).

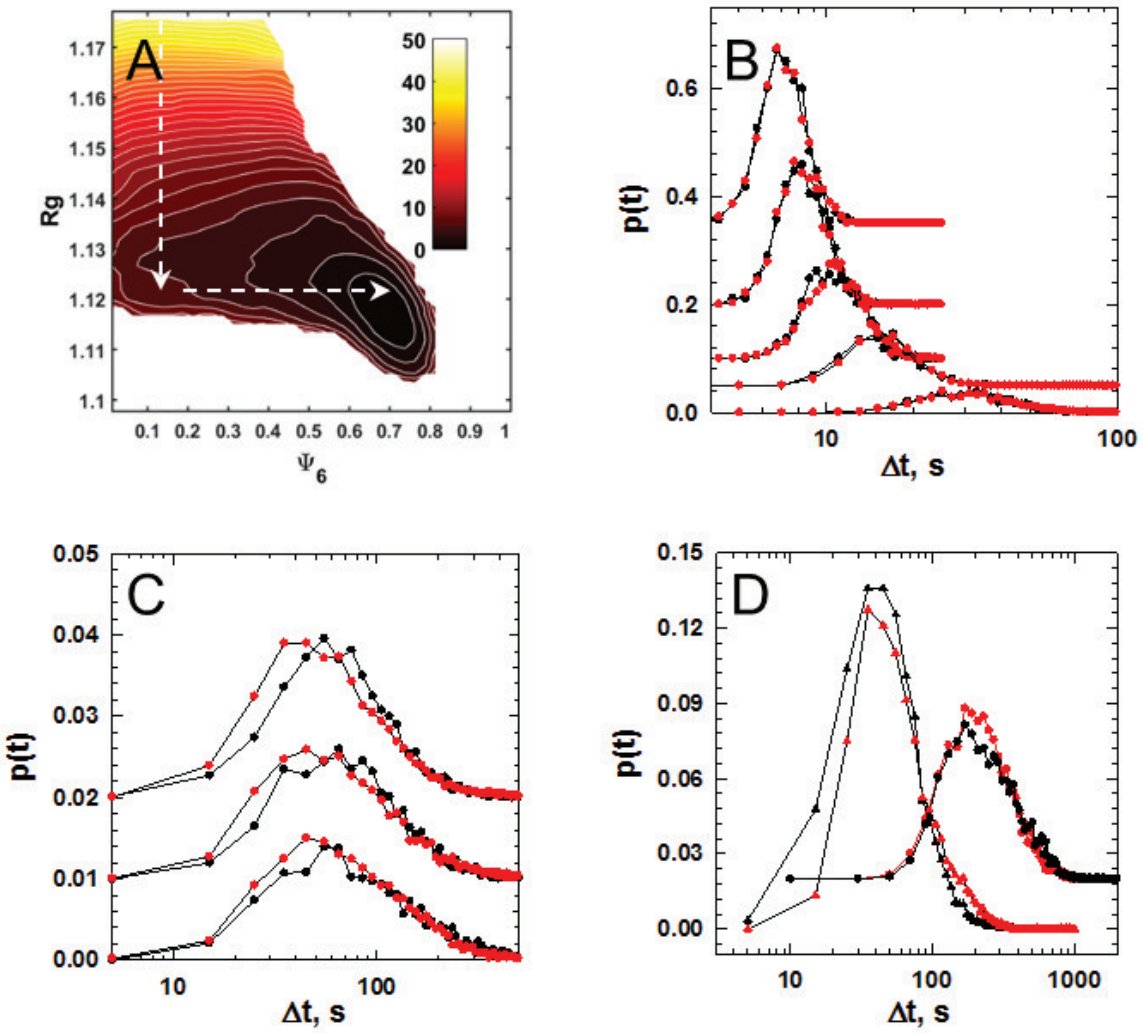


Figure 3.11: First passage time distribution (FPTD) comparisons between BD (black) and LDLD (red) trajectories.(A) Vertical arrow denots condenstation along the steep free energy gradient and horizontal arrow denotes grain boundary migration along the free energy plateau. (B) FPTD for condensation process for initial and final $R_g$ states between (top to bottom curves): (1.24,1.22), (1.22,1.20), (1.20,1.18), (1.18,1.16), and (1.16,1.14). (C) FPTD for grain boundary migration for initial and final $\psi_6$ states between (top to bottom curves): (0.4,0.6), (0.3,0.5), and (0.2,0.4). (D) FPTD corresponding to T1 and T2 in Fig. 3.10 between a sink at $\psi_6 = 0.7, R_g = 1.18$ and sources at $\psi_6 = 0.15, R_g = 1.13$ (circles) and $\psi_6 = 0.5, R_g = 1.14$ (triangles).

After showing the accuracy of the LDLD model via first passage time distributions, it is possible to completely explore the dynamic evolution of the system by using the low dimensional models in Fig. 3.10 to numerically solve the Smoluchowski equa-

tion. This provides more complete information on the time evolution of states during stochastic assembly processes (e.g. compared to first passage times alone). Fig. 3.12 shows the solution of SE ($p(x,t)$) at different voltages and observation times $\Delta t$, with given initial conditions, $p(x,0) = \delta(x - x_0)$, $x_0 = (0.025, 1.22)$, which corresponds to an initial fluid configuration.

At the lowest voltage, Figs. 3.12(A),(B) show that the evolution of $p(x, \Delta t)$ is characterized by slow drift and diffusion of the initial delta function towards the new equilibrium state, which is a broader distribution of configurations centered on a more condensed fluid like state. Convergence to the equilibrium Boltzmann distribution is observed to occur within 200 s (most easily seen from blue and cyan curves in Fig. 3.12(B)). At the intermediate voltage, Figs. 3.12(C),(D) show how $p(x, \Delta t)$ drifts rapidly towards more condensed and ordered states before a loosely packed crystal state emerges between 100-200 s and the equilibrium distribution is reached within $\sim$ 400 s. At the highest voltage, which corresponds to conditions when a single crystal is expected as the global free energy minimum configuration, Figs. 3.12(E),(F) show how $p(x, \Delta t)$ drifts even more rapidly toward evolving ordered configurations that once again reach the equilibrium distribution in $\sim$ 400 s. The results in Fig. 3.12 show how the low-dimensional model captures the stochastic evolution of the probability density of states at different thermodynamic conditions, which captures all dynamic information necessary to design, control, and optimize colloidal assembly schemes in this system.

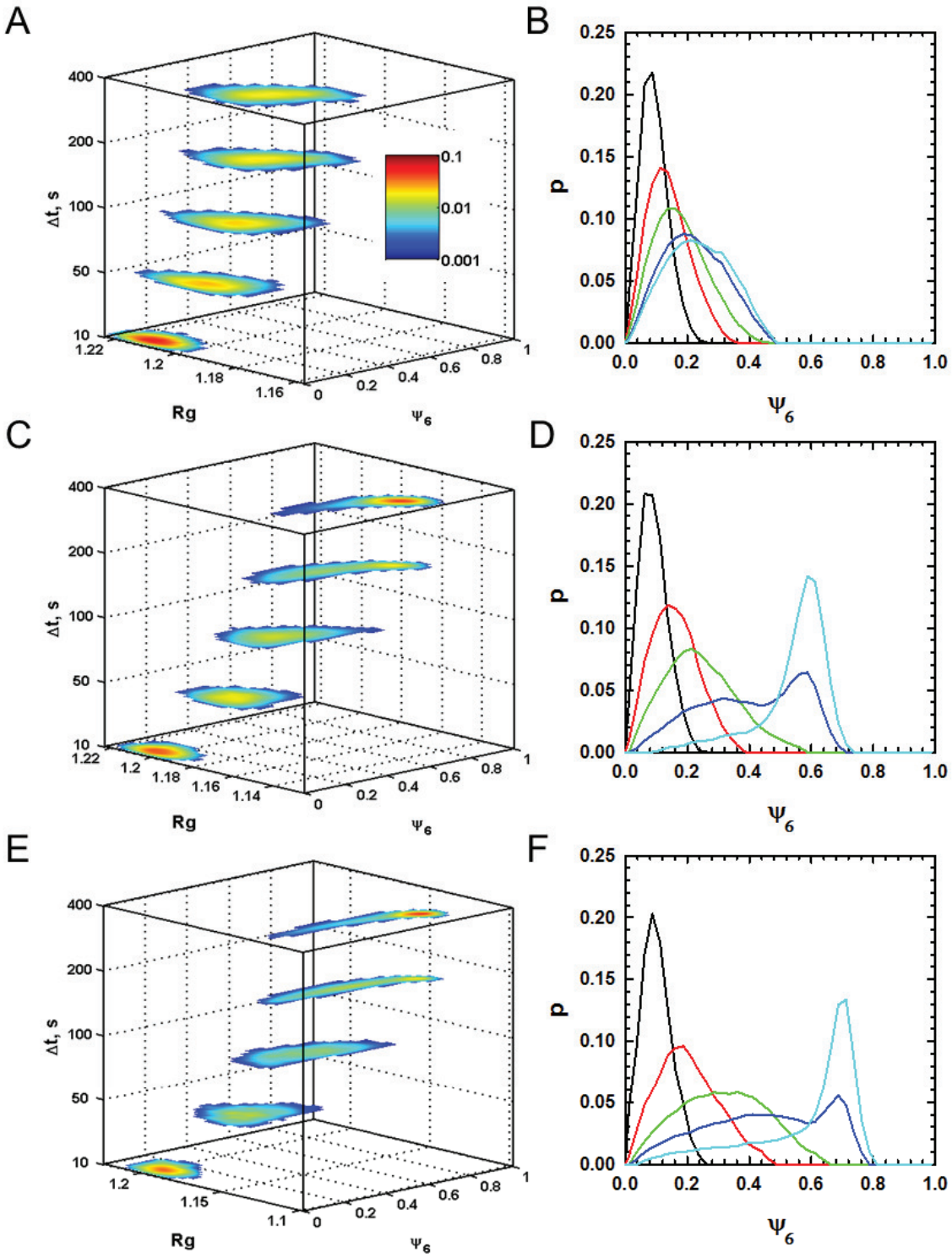


Figure 3.12: Numerical solution of the Smoluchowski equation to calculate $p(\mathbf{x}, t)$ at observation times $\Delta t$ = 10 s, 100 s, 200 s, and 400 s at applied voltage (A),(B) $V^*$ = 0.42 (C),(D) $V^*$ = 0.50 (E),(F) $V^*$ = 0.57. Initial conditions for all cases is $p(\mathbf{x}, 0) = \delta(\mathbf{x} - \mathbf{x}_0)$, $\mathbf{x}_0 = (\psi_6, R_g) = (0.025, 1.22)$. The left column are 2D contour plots of $p(\mathbf{x}, t)$ and right column are 1D projections onto the $\psi_6$ coordinate for $\Delta t$ = 10 s (black), 50 s (red), 200 s (blue), and 400 s (cyan).

## 3.4 Summary & Conclusions

We investigated the phase behavior of a system of quasi-2D colloidal silica particles confined within quadrupole electrodes in an inhomogeneous electric field. We applied diffusion maps to probe the formation of defective microstructures and how these defects migrate to the edge of the structure to form perfect crystals. Diffusion maps picked up the condensation as the key feature of the assembly as confirmed by the excellent correlation $R_g$ showed with the eigenvector. However the migration of defects were not captured and $\psi_6$ showed a very poor correlation with the eigenvector. The Hausdorff distance metric, a key aspect of the diffusion maps technique in constructing the Markov matrix failed to distinguish between defective crystals that contained grain boundaries and perfect crystals. We added a second term to the distance metric that is sensitive to the local orientation of the neighbors around each particle in the cluster and this helps in detecting defects in the crystal. Application of diffusion maps with the modified distance metric improved the correlations of eigenvector with $\psi_6$. Free energy and diffusivity landscapes were built in the coarse variable space $(R_g, \psi_6)$ and the low dimensional Langevin dynamics were benchmarked with full scale BD simulations. The interesting physics of this system is the condensation along the steep free energy gradient in the $R_g$ direction and the migration of the grain boundaries along the free energy plateau in the $\psi_6$ direction and both of these aspects are captured very well by the mean first passage time distributions as well as the numerical solution of the governing Smoluchoswski equation for this assembly process.

# CHAPTER 4

# THERMODYNAMICS OF COLLOIDAL CLUSTERS: DEPLETION SYSTEM REVISITED

## 4.1 Introduction

The central theme of the previous chapters was modeling self-assembly and phase behavior of colloidal clusters using an order-parameter approach. Diffusion mapping was used to locate an underlying low-dimensional manifold, and a heuristic procedure was used to identify an appropriate set of OPs. We then built free energy and diffusivity landspaces to determine the equilibrium and dynamical properties of these small clusters. Using this approach, free energy landscapes and phase diagrams have been generated for different system sizes and range of pair-potential in [57, 58].

In contrast to the order parameter approach, here we explore the phase behavior of the depletion potential system via a histogram-based simulation approach. We conducted replica exchange Monte Carlo simulations of these small colloidal clusters and generated potential energy histograms at different values of the osmotic pressures. From the framework of thermodynamics for small systems [59], a single peak in the histogram corresponds to a single stable phase and a double peak corresponds to two coexisting phases in equilibrium. Certain intermediate values of the osmotic pressure yielded fluid-solid coexistence. We present a quantitative analysis of these histograms and construct phase coexistence curves for these small clusters. We investigate the phase behavior for different cluster sizes at a fixed depletant size and vary the depletant density to control the strength of the attraction. The parameters involved in this pair-potential can be found in Eq. 2.1.

We discuss the simulation methodology used to generate the potential energy histograms followed by analysis of the energy histograms for different osmotic pressures. We then compute the phase coexistence curves from the energy histograms and compare them to calculations from the FEL approach.

## 4.2 Replica Exchange Monte Carlo Simulations

Results from initial canonical Monte Carlo studies suggested that an enhanced sampling algorithm would be benificial in generating the potential energy histograms. First we review the algorithm that we chose (parallel tempering) and then describe how we implemented it.

Parallel tempering, or replica exchange simulation technique [60] is a method where a given number of replicas are simulated, typically in canonical ensemble at a series of temperatures. Replicas at adjacent temperatures are swapped at a certain frequency based on an acceptance criterion. The high temperature replicas sample a larger volume of phase space while the low temperature replicas may get trapped in a metastable state and an exchange of information between replicas enables good sampling of the entire phase space.

The idea of the parallel tempering technique is however not limited to exchanges between replicas at different temperatures or the number of parameters in which the tempering can be performed. de Pablo and co-workers [61] have performed hyper-parallel tempering methods in the grand canonical ensemble by making exchanges between replicas at different temperatures and chemical potentials. They have also studied large polymeric systems in an expanded grand canonical framework [62] where in addition to temperature and chemical potential, the length of the polymeric chain in the replicas is also a parameter used for tempering. Fukunishi *et al.* [63] developed a Hamiltonian parallel tempering method which was applied to biomolecular systems wherein each replica of the system has different interaction potentials. We

have invoked this idea of Hamiltonian replica exchange method and applied it to the depletion potential system and details of its implementation follow.

We fix the temperature of each replica and vary the depletant concentration across the replicas. This implies a series of replicas with different Hamiltonians varying in depth of the attractive potential well and the depth is determine by the osmotic pressure $\Pi^*$ of each replica. Since the temperature is fixed for all the replicas, the size of depletant is the same and hence the range of the pair potential stays constant across replicas. The parallel tempering scheme described here is shown in Fig. 4.1 where the osmotic pressure due to the depletants are shown as varying shades of background color in each replica. The acceptance criteria for the Hamiltonian replica exchange method for a swap between replicas $i$ and $j$ is given by [60],

$$A = \min\left\{1, \exp\left[-\beta\left(\left[H_i(X') + H_j(X)\right] - \left[H_i(X) + H_j(X')\right]\right)\right]\right\} \tag{4.1}$$

where $H_i(X)$ is the Hamiltonian of configuration $X$ in replica $i$, and configurations $X$ and $X'$ are the configurations in replicas $i$ and $j$, respectively, before the swap is made.

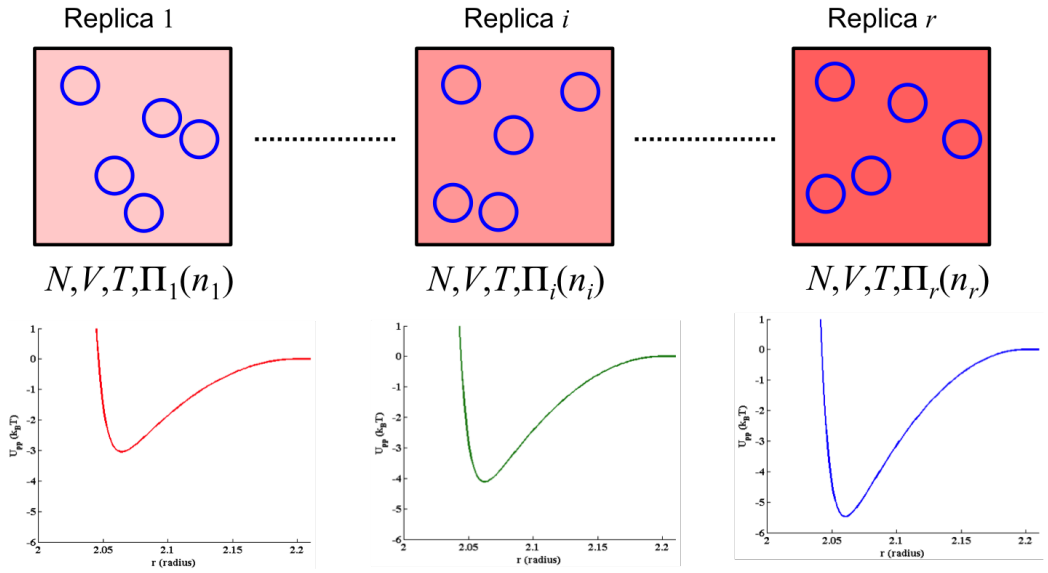


Figure 4.1: Hamiltonian replica exchange scheme for the depletion potential system shows two replicas with different levels of interparticle attraction as can be seen in the pair potential curves. The intensity of the background color is a measure of the osmotic pressure strength due to the differing levels of depletant concentration in the replicas.

## 4.3 Potential Energy Histograms & Analysis

We conducted replica exchange Monte Carlo runs for the parameters $N = 32$ and $L = 110$ nm since we have extensive data available from previous studies [49, 52, 57, 58] based on the order parameter approach to compare our calculations. We initially conducted runs of 100 parallel tempering steps with $10^6$ canonical Monte Carlo steps in between each parallel tempering step. These initial runs provide an estimate of the operating window of osmotic pressure in which there is phase coexistence. We have summarized the results of these runs in Fig. 4.2. Fig. 4.2(a) shows histograms for four osmotic pressures. The histogram distributions for the lowest three osmotic pressures resemble a Gaussian centered around $U \sim -130\ k_BT$ and this high-energy fluid-like configurations within the Gaussian is the only stable phase at these $\Pi^*$ values. We note from Fig. 4.2(a) the presence of a small peak centered around $U \sim$

-360 $k_BT$. This is a low-energy solid-like condensed phase that is metastable relative to the stable fluid-like phase.

Fig. 4.2(b) shows the energy distributions for a slightly higher range of osmotic pressures and all the histograms shown here are double-peaked indicative of the phase coexistence regime. The fluid-like phase is more stable for the lower two $\Pi^*$ while the solid-like phase is more stable for the higher two $\Pi^*$. Based on these histograms, we could infer that the osmotic pressure at which both phases are equally likely to be found lies between the values corresponding to the green and black curves. Fig. 4.2(c) show the energy distributions for the third set of osmotic pressures. We observe in Fig. 4.2(c) that solid-like phase is the most stable phase over the entire range of $\Pi^*$ and fluid-like phase is metastable.

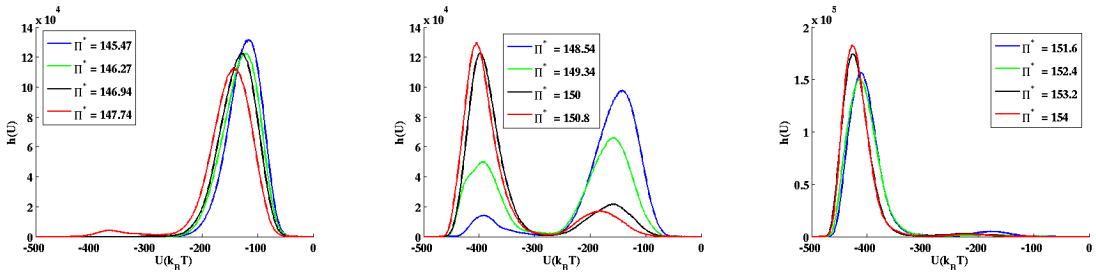


(a) Energy histograms for $\Pi^* = 145.47$ (blue), $\Pi^* = 146.27$ (green), $\Pi^* = 146.94$ (black), $\Pi^* = 147.74$ (red).

(b) Energy histograms for $\Pi^* = 148.54$ (blue), $\Pi^* = 149.34$ (green), $\Pi^* = 150$ (black), $\Pi^* = 150.8$ (red).

(c) Energy histograms for $\Pi^* = 151.6$ (blue), $\Pi^* = 152.4$ (green), $\Pi^* = 153.2$ (black), $\Pi^* = 154$ (red).

Figure 4.2: Potential energy histograms for $N = 32$ particle cluster generated across a series of $\Pi^*$ values using replica exchange Monte Carlo simulations. (a) Fluid-like phase is the most stable phase and we observe onset of a solid-like low-energy phase for one of the $\Pi^*$ (red curve) (b) Both fluid-like and solid-like observed in significant amounts for all 4 $\Pi^*$ simulated and we notice an exchange of stability in this range of $\Pi^*$ (c) Solid-like phase is the most stable and fluid-like phase gradually disappears for higher $\Pi^*$.

Fig. 4.3 shows the corresponding trajectory of the osmotic pressures through the various processors during the course of the parallel tempering simulation. We record histogram statistics by following the trajectory of every individual $\Pi^*$ and calculate

the energy distributions for each one of the $\Pi^*$ shown in Fig. 4.2. Fig. 4.3(a) shows the trajectory for the histograms in Fig. 4.2(a) and this run had an acceptance ratio of 84%. Since all the histograms reside in similar energy ranges, a high percentage of the swap moves are accepted as observed in Fig. 4.3(a).

In Fig. 4.3(b) we observe that the number of swaps made are lower than the one for Fig. 4.3(a). Since the histograms are all double-peaked, configurations in adjacent replics could be found in either of the two peaks and the energetic penalty can be too high for a swap to be accepted. We see that after $\sim$ 50 parallel tempering steps, the swaps are made only between two sets of adjacent osmotic pressures (blue with green and red with black). This leads to a lower acceptance of 62%. Energy histograms in Fig. 4.3(c) all reside in the low-energy regions thus leading to a high acceptance ratio of 84% for the run shown in Fig. 4.3(c).

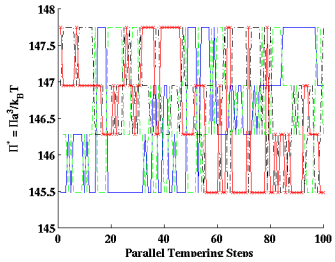


(a) $\Pi^* = 145.47$ (blue), $\Pi^* = 146.27$ (green), $\Pi^* = 146.94$ (black), $\Pi^* = 147.74$ (red).

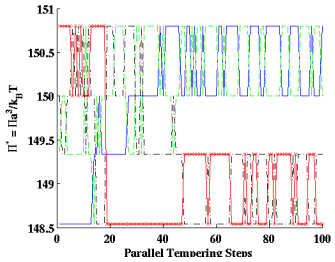


(b) $\Pi^* = 148.54$ (blue), $\Pi^* = 149.34$ (green), $\Pi^* = 150$ (black), $\Pi^* = 150.8$ (red).

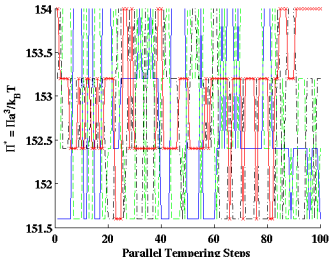


(c) $\Pi^* = 151.60$ (blue), $\Pi^* = 152.40$ (green), $\Pi^* = 153.20$ (black), $\Pi^* = 154$ (red).

Figure 4.3: Osmotic pressure trajectory over the course of the replica exchange Monte Carlo simulations. For cases (a) and (c) the energy histograms are centered around either high-energy or low-energy ranges and thus the likelihood for swap acceptance is high. The acceptance ratio is 84% for both cases. Since energy histograms for (b) contain twin peaks and the energetic penatly for swap acceptance is higher and this leads to acceptance of 62%, lower than (a) and (c).

## 4.4 Phase Coexistence Curves

This histograms presented in the previous section provided an estimate of the osmotic pressure range over which we observe phase coexistence. We ran longer Monte Carlo runs with a thousand parallel tempering steps with a million canonical Monte Carlo steps after each tempering step. We chose 20 replicas and a corresponding set of osmotic pressure values that spanned the entire range of phase coexistence. We calculated the distribution metric $D$ from the energy histograms as follows.

The relative stability of two phases A and B (manifest as twin peaks in an energy histogram) can be quantified using the distribution metric D from [23] given by

$$D = \frac{K-1}{K+1};\ K = \frac{[A]}{[B]} \tag{4.2}$$

where K is the equilibrium ratio of the amounts of A and B. D = -1 corresponds to pure B and D = 1 to pure A. Any value of $D\ \epsilon\ [-1, 1]$ implies coexistence of A and B. We calculate $D$ from the relative areas in the peaks of the potential energy histograms to construct phase diagrams for these small colloidal clusters.

These calculations were performed for cluster sizes $N = 25, 27, 30, 32$ and the distribution metric $D$ as a function of the osmotic pressure $\Pi^*$ is shown in Fig. 4.4. For low osmotic pressures, the clusters for all system sizes sample the only fluid-like phase ($D = -1$). The onset of solid-like crystalline phase is first observed for $N = 32$. With increase in $\Pi^*$, the cluster undergo a transition from a fluid-dominated phase ($D < 0$) to a solid-dominated phase ($D > 0$). The onset of solid-like crystalline phase is delayed for smaller cluster sizes. The transition curve is more diffuse for smaller clusters and the width of the coexistence region (range of $\Pi^*$) increases. From this figure, we note that $\Pi^*$ can be varied to control the stability and the relative amounts of the two phases in equilibrium.

We compare the phase coexistence curves shown in Fig. 4.4 with the order parameter approach studied in Chapter 2. In order to quantify the relative amounts of

different phases in the FELs, we invert the free energy to a probability measure by using

$$P(\mathbf{\Psi}) \propto \exp\left[-\frac{W(\mathbf{\Psi})}{k_B T}\right] \tag{4.3}$$

where $P(\mathbf{\Psi})$ is the probability of observing the system in a state $\mathbf{\Psi}$ and $W(\mathbf{\Psi})$ is the FEL. Specific to this colloidal system, we observe a fluid-like phase in coexistence with a solid-like phase and thus we sum up the probabilities in both these basins and compute $D$ using Eq. 4.2.

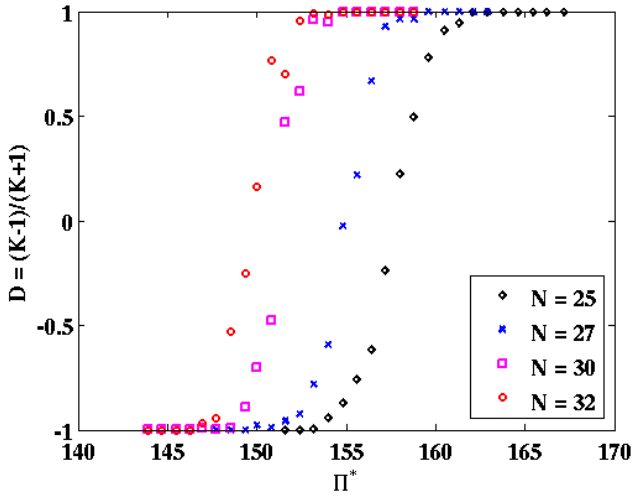


Figure 4.4: Phase coexistence curves shown for system sizes $N = 25$ (black), 27 (blue) ,30 (magenta), and 32 (red). The curves indicate a transition from a fluid-dominated phase ($D < 0$) to a solid-dominated phase ($D > 0$). The transition curves also becomes more diffuse and coexistence region widens as the size of the cluster decreases.

The FEL analysis has been performed for the $N = 32$ system and shown in Fig. 4.5 (magenta symbols). We have also plotted the phase coexistence data from Fig. 4.4 corresponding to $N = 32$ (red symbols). We observe a very good qualitative and a reasonable quantitative agreement between the order parameter FEL approach and the potential energy histogram method. From fundamental thermodynamics, we have used potential energy as a metric to capture the phase changes in small colloidal

clusters and the phase coexistence curves agree very well with a more sophisticated order parameter approach studied in Chapter 2. It is also interesting to note here that such phase changes have been observed in experimental works. Dinsmore and co-workers have observed two-step mechanisms of sublimation and crystallization that involve fluid-solid transitions in small colloidal clusters [13, 64]. DNA-coated gold-nanoparticles and colloidal systems show a similar phase behavior over a range of temperature that controls the hydrogen bond strength between the DNA strands [65–67]. Phase coexistence curves such as shown in Fig. 4.4 provide a fundamental understanding of phase changes in colloidal particle assemblies.

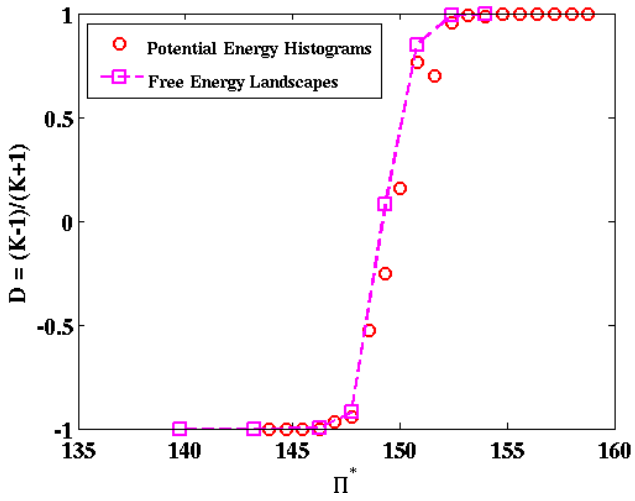


Figure 4.5: Comparison of the phase coexistence curves shown for $N = 32$.

An alternate way to plot phase coexistence is by constructing a $P - v$ type phase diagram. The phase diagrams for bulk colloidal systems are traditionally plotted in the space of volume fraction of large colloidal and small depletant spheres. Fig. 4.6 shows the phase diagram for a bulk colloidal system expressed as a $\eta_s^r - \eta_l$ plot [68]. In this plot, $\eta_s^r$ is the volume fraction of the depletants while $\eta_l$ is the volume fraction of the large colloidal particles. We see both single phase and two phase regions separated by the phase coexistence curves for a depletant colloid size ratio

of 0.1. A key difference between bulk systems and small clusters is the lack of a definition of a homogeneous volume or density for the latter. We propose here to use $(R_g)^3$ as a proxy measure for the volume of the clusters since radius of gyration has proven to be a good measure of condensation in the order parameter study. We have plotted $\Pi^*$ against $(R_g)^3$ in Fig. 4.7(a) and $(R_g)^{-3}$ in Fig. 4.7(b). Figs. 4.7(a) and 4.7(b) resemble a typical pressure-volume or pressure-density plot with the fluid and the solid branches (blue symbols) on either side of the coexistence region that is shaded. The red symbols in Fig. 4.7 correspond to coexistence of fluid-like and solid-like phases over a range of $\Pi^*$.

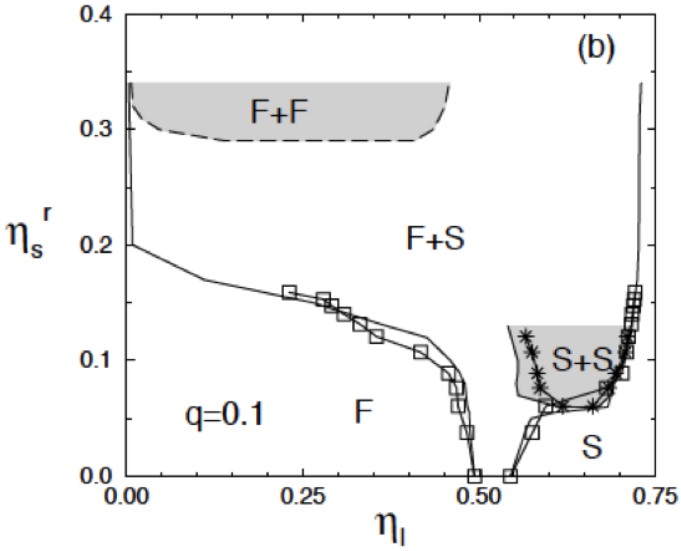


Figure 4.6: Bulk phase diagram for the depletion potential system from [68]. $\eta_l$ is the volume fraction of large colloids while $\eta_s^r$ is the volume fraction of the reservoir of small depletants.

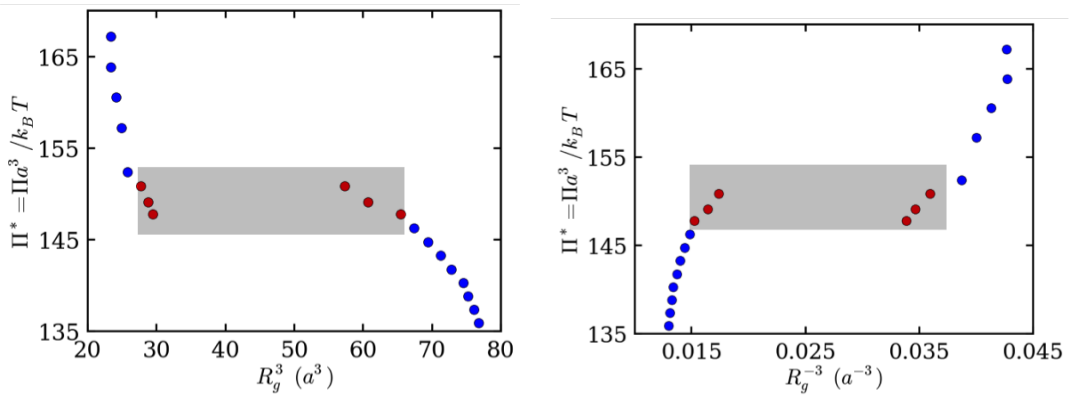


(a) $\Pi^*$ vs $R_g^3$ plot for colloidal cluster with $N = 32$ from MC simulations.

(b) $\Pi^*$ vs $R_g^{-3}$ plot for colloidal cluster with $N = 32$ from MC simulations.

Figure 4.7: Phase coexistence curves expressed as (a) $\Pi^* - (R_g)^3$ and (b) $\Pi^* - (R_g)^{-3}$ for $N = 32$ system.

## 4.5 Summary & Conclusions

We have revisited the depletion potential system and studied its phase behavior using a histogram-based simulation approach. We conducted replica exchange Monte Carlo simulations using the osmotic pressure as the tempering variable. We generated potential energy histograms that captured the fluid-solid phase coexistence by carefully tuning the osmotic pressure. We constructed phase coexistence curves by calculating the distribution metric $D$ from the energy histograms. These coexistence curves showed good agreement with the FELs generated using the order parameter approach. We also made $\Pi^* - (R_g)^3$ plots analogous to $P - v$ plots for bulk systems and highlighted the key difference between bulk and thermodynamically small systems.

# CHAPTER 5

# SUMMARY & FUTURE RESEARCH DIRECTIONS

## 5.1 Summary

We have studied the directed assembly of two model colloidal systems by building reduced-dimension process models that link the particle-level dynamics of the colloids to the actuator states. We have developed a three-part strategy for developing such process models. First, we employed diffusion mapping on raw trajectory data to identify slow, low-dimensional manifolds in the system dynamics. Second, we identified convenient observables, or order parameters, that showed strong correlation with low-dimensional DMap coordinates. Finally we used the Smoluchowski equation to build free energy and diffusivity landscapes that serve as reduced-dimension process models to describe the system's thermodynamics and kinetics respectively. An optimal control policy map is computed using dynamic programming in the DMap coordinates. This control policy map along with the landscape models aid in the optimal feedback controlled assembly of perfect colloidal crystals[69].

One of the key findings of this thesis is the importance of the choice of distance metric for the success of the diffusion mapping technique. We used Hausdroff distance metric for both the systems. For the depletion potential case, Hausdroff distance was able to distinguish between both fluid and solid phases as well as single and broken clusters in the solid phase. This was manifest in the correlations observed with average cluster to cluster distance metric. For the quadrupole system, while Hausdorff distance metric could detect differences between expanded and condensed structures, it showed no sensitivity towards the presence of grain boundaries found in

polycrystalline microstructures. This led to the modification of the distance metric to account for local orientation of neighbors around each particle and this improved the correlation of $\psi_6$ against the eigenvectors. DMap analysis of two different systems revealed the importance of distance metric in identifying the best possible coarse-variables to build the low-dimensional models.

We have also built phase coexistence curves for small clusters by quantitative analysis of potential energy histograms generated using replica exchance Monte Carlo simulations. These histograms highlighted the idea of dynamic phase coexistence in thermodynamically small systems which show frequent transitions between phases whose relative free energy difference vary by a few $k_BT$. We have compared these calculations with the order parameter approach and observed a very good agreement between the two methods.

## 5.2 Estimation of Free Energies using Biased Sampling Techniques

In this thesis, we have extensively used Monte Carlo umbrella sampling as our engine for performing free energy calculations in a given order parameter phase space. When we applied this technique to the field assembly problem, we observed insufficient sampling in the biasing windows in regions of high free-energy, despite running long MC trajectories. Such insufficient sampling leads to inaccurate estimates of free energies and also a lack of representative configurations in OP space. Such equilibrated configurations serve as vital starting points in OP space to initiate dynamic simulations and build Smoluchowski models from the resulting trajectories.

Thus, we use an alternate form of biased sampling to estimate free energies across the whole range of OP space and produce equilibrium configurations. To be more specific, we alter the Metropolis criterion by incorporating additional biasing functions to promote uniform sampling across the entire span of OP values and follow it up

with reweighting techniques. For such biased sampling techniques, the acceptance criterion is

$$P_{12} = \min\{1, \exp(-\beta\Delta U_{12} + \Delta\eta_{12})\} \tag{5.1}$$

where $\eta$ is the biasing function. We run multiple MC simulations using approximations of the bias function to sample a wide range of overlapping OP values. Using the histograms recorded from each simulation and the corresponding bias function, we construct a single bias function over the entire range of OP values sampled. This resulting bias function can then be used to drive the simulations and sample a wide range of OP values. This is an iterative process and the biasing function is continuously updated until the entire physical range of OP values are sampled.

Fig. 5.1 is the radius of gyration $R_g$ histogram obtained from an unbiased MC simulation at a voltage $V^* = 0.3$. At this low voltage, the natural state of the system is fluid-like and the $R_g$ range sampled is roughly over the interval [13.2, 14.2]. In order to sample more condensed states at this voltage, we require a high free energy penalty to drive the system to sample lower $R_g$ values. Fig. 5.2 is one example of a biasing function at the voltage value $V^* = 0.3$. This biasing function is constructed from a set of multiple bias functions that were used in independent MC simulations. Application of this bias results in a roughly uniform sampling of the $R_g$ space as shown in Fig. 5.3.

There are two useful products from this process, for a fixed voltage in the quadrupole apparatus. The first is an accurate FEL across the entire OP space. The second is a set of particle configurations across the entire OP space, which should be representative of equilibrium conditions at the fixed voltage.

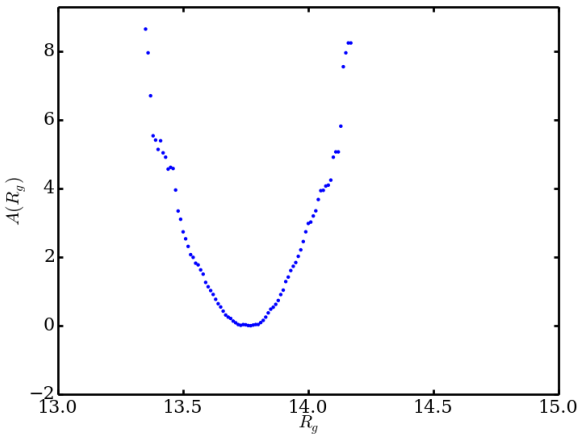


Figure 5.1: Histogram sampling from an unbiased Monte Carlo simulation at a voltage $V^* = 0.3$.

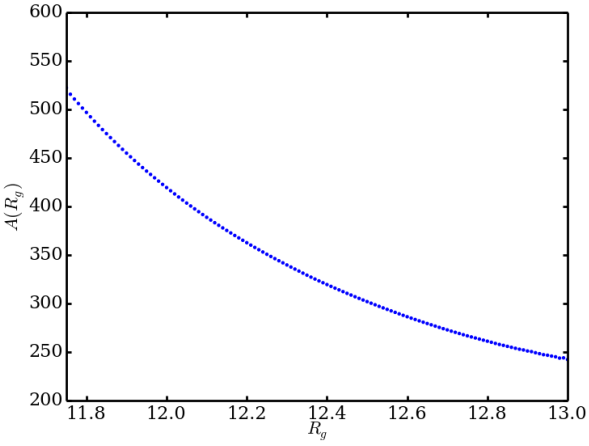


Figure 5.2: Biasing potential $A(R_g)$, constructed from a set of independent Monte Carlo simulations.

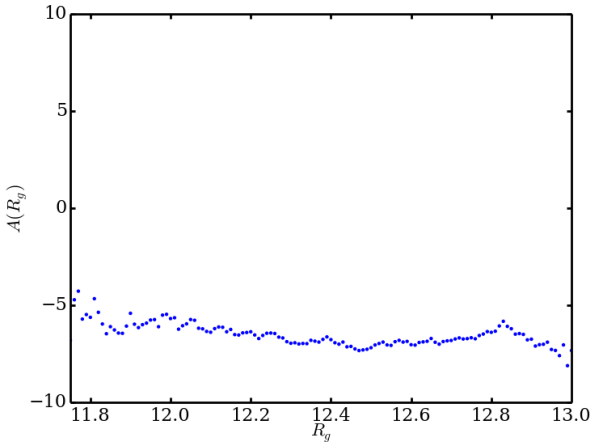


Figure 5.3: Histogram resulting from the application of the biasing function. Biasing promotes uniform sampling over the entire range of $R_g$ shown.

Biased sampling for two more voltage levels, $V^* = 0.5$ and $V^* = 0.7$ will produce equilibrium configurations across a wide range of $R_g$ values at three voltage levels. Additional order parameter calculations ($\langle C_6 \rangle, \psi_6$) will determine if there are microstructural differences across these equilibrium configurations. The reason for producing and comparing these configurations is discussed below.

Dynamic models (diffusivity landscapes) are built by initiating local trajectories from configurations in OP space and estimating the Smoluchowski equation coefficients[50]. We wish to examine if certain characteristics of the configurations (like the voltage at which it was produced and its location in OP space) has an impact on the estimation procedure. To this end, we will use a bunch of configurations produced from the biased sampling technique to initiate trajectories and examine the resulting diffusivity landscapes. Differences would have implications on key assumptions (eg. Markovian nature of the colloidal assembly process) underlying the process of building these landscape models.

## 5.3 Equilibrium Crystal Shapes and Morphology of Lennard-Jones Clusters

In addition to studying colloids, we also investigate the phase behavior of small Lennard-Jones clusters. The structures and potential energy landscapes of small Lennard-Jones clusters has been very well studied and global minimum energies of some of these clusters have been reported in [70]. Such small clusters exhibit qualitatively different structural and phase behavior compared to the corresponding bulk systems. Previous work from my research group [71] focused on the $LJ_{38}$ cluster which exhibits very rich phase behavior characteristics with fluid-solid and solid-solid phase transitions [72, 73]. The work in [71] involved the use of diffusion mapping to justify a coarse grained model which was able to capture the polymorphic solid-solid transitions at low temperatures and melting transitions at higher temperatures.

A fundamental understanding of the equilibrium structures and morphology of small clusters is essential for further studies on the thermodynamics and kinetics of crystal nucleation and growth. Towards this end, the first step is to compute ground-state energies and morphologies of various crystal assemblies as a function of system size. Recent work from our research group [74] has focused on studying the equi-

librium crystal shapes of colloidal crystals using the classical Wulff construction [75] as well as a generalization of that technique. While the traditional Wulff technique works well for system sizes that are nearly bulk (comprising tens of thousands of particles or higher), a novel generalized technique was developed and implemented to explicitly handle small clusters containing few tens of particles where surface effects are important. We use this technique to explore the equilibrium structures and morphologies of small LJ clusters.

The generalized Wulff constructions consists of a set of lattice-site-exchange Monte Carlo simulations coupled with a parallel tempering scheme. Each simulation run produces a minimum-energy configuration for a given system size and a choice of the underlying crystalline lattice. More details about the generalized Wulff algorithm can be found in recent work by our coworkers [74]. We ran the generalized Wulff construction for LJ clusters upto $N = 110$ for both FCC and HCP lattice structures and have reported the minimum energies for each cluster size. We have plotted cohesive energy per particle as a function of cluster size in Fig. 5.4. We have also plotted the global minima of LJ clusters reported in literature [70] for comparison with the generalized Wulff technique results. We observe that our results capture the trend in global minima qualitatively for the entire size range examined here. The agreement is excellent up to $N \sim 35$ beyond which the minimum-energies are lower (in magnitude) compared to the global minima. We have also examined the stability of the clusters by computing the second-order energy difference defined as,

$$\Delta_2(N) = E_b(N+1) + E_b(N-1) - 2E_b(N) \tag{5.2}$$

where $E_b(N)$ is the binding energy of a cluster of size $N$. This metric identifies the so called magic clusters which show improved stability over similarly sized clusters. We have computed $\Delta_2(N)$ as a function of $N$ for both FCC and HCP lattice structures and compared them with the magicity of the global minima clusters in Fig. 5.5 shows

the comparisons of magicity. Similar to the minimum-energy curve, we observe very good agreement in magicity for both FCC and HCP lattice types with the global minima clusters upto $N \sim 35$.

The generalized Wulff construction is a technique that consists of lattice-site-exchange moves followed by configurational relaxation Monte Carlo runs. We have been able to calculate minimum-energy configurations and also predict magicity of clusters for $N$ upto 35. We however underpredict the global minima energies consistently for higher cluster sizes. One way to improve the algorithm is to introduce a a shear (displace the lattice plane) prior to the configurational relaxation step. The ultimate objective of this exercise is to use the generalized technique (which is easy to implement and also an effective technique) to identify minimum-energy clusters for a wide size range and characterize their morphologies and compare and constrast with the vast database of LJ clusters available in literature [70].

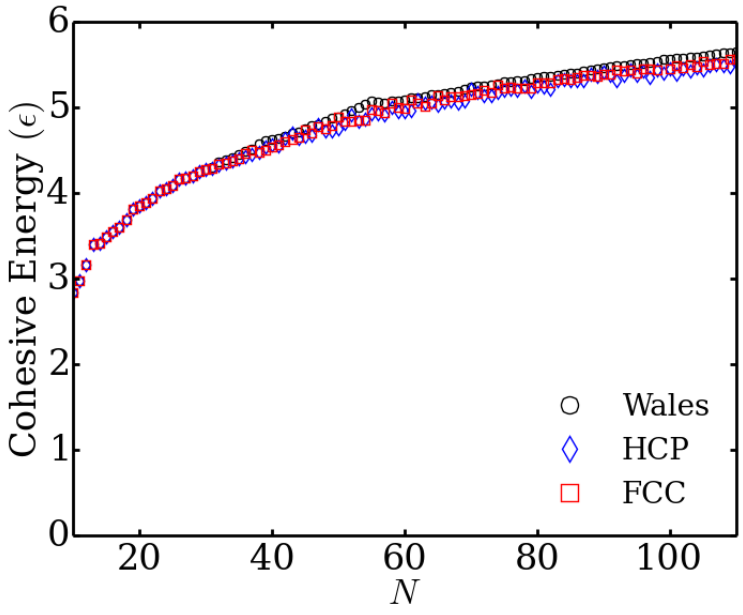


Figure 5.4: Minimum-energy clusters from for FCC and HCP lattice structures from generalized Wulff construction for cluster sizes upto $N = 110$ atoms. We have also compared the energies with global minima reported in literature [70]. Excellent agreement is seen for cluser sizes upto $N \sim 35$ beyond which this the minimum energy is lower in magnitude when compared to the global minima.

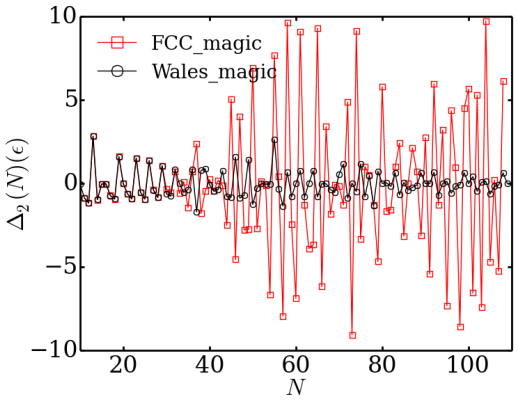


(a) FCC compared with global minima structures.

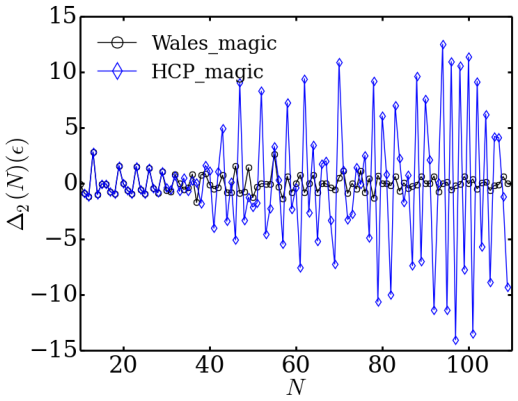


(b) HCP compared with global minima structures.

Figure 5.5: Comparison of stability of clusters between FCC, HCP and global minima structures. The magicity of stable clusters is well predicted for sizes upto $N \sim 35$.

# BIBLIOGRAPHY


[1] J. D. Joannopoulos, P. R. Villeneuve, and S. Fan, Photonic crystals: putting a new twist on light, *Nature* **386**(6621), 143–149 (1997).

[2] N. Engheta, Circuits with light at nanoscales: optical nanocircuits inspired by metamaterials, *Science* **317**(5845), 1698–1702 (2007).

[3] E. Yablonovitch, Photonic crystals: semiconductors of light, *Scientific American* **285**(6), 46–55 (2001).

[4] G. M. Whitesides and B. Grzybowski, Self-assembly at all scales, *Science* **295**(5564), 2418–2421 (2002).

[5] G. M. Whitesides and M. Boncheva, Beyond molecules: Self-assembly of mesoscopic and macroscopic components, *Proceedings of the National Academy of Sciences* **99**(8), 4769–4774 (2002).

[6] M. Grzelczak, J. Vermant, E. M. Furst, and L. M. Liz-Marzán, Directed self-assembly of nanoparticles, *ACS Nano* **4**(7), 3591–3605 (2010).

[7] F. Li, D. P. Josephson, and A. Stein, Colloidal assembly: the road from particles to colloidal molecules and crystals, *Angewandte Chemie International Edition* **50**(2), 360–388 (2011).

[8] O. D. Velev and S. Gupta, Materials fabricated by micro-and nanoparticle assembly–the challenging path from science to engineering, *Advanced Materials* **21**(19), 1897–1905 (2009).

[9] A. van Blaaderen and P. Wiltzius, Growing large, well-oriented colloidal crystals, *Advanced Materials* **9**(10), 833–835 (1997).

[10] T. Biben, R. Ohnesorge, and H. Löwen, Crystallization in sedimentation profiles of hard spheres, *Europhysics Letters* **28**(9), 665 (1994).

[11] A. Yethiraj, J. H. Thijssen, A. Wouterse, and A. van Blaaderen, Large-area electric-field-induced colloidal single crystals for photonic applications, *Advanced Materials* **16**(7), 596–600 (2004).

[12] T. Solomon and M. J. Solomon, Stacking fault structure in shear-induced colloidal crystallization, *The Journal of Chemical Physics* **124**(13), Article No. 134905 (2006).

[13] J. Savage, D. Blair, A. Levine, R. Guyer, and A. Dinsmore, Imaging the sublimation dynamics of colloidal crystallites, *Science* **314**(5800), 795–798 (2006).

[14] G. E. Fernandes, D. J. Beltran-Villegas, and M. A. Bevan, Interfacial colloidal crystallization via tunable hydrogel depletants, *Langmuir* **24**(19), 10776–10785 (2008).

[15] G. E. Fernandes, D. J. Beltran-Villegas, and M. A. Bevan, Spatially controlled reversible colloidal self-assembly, *The Journal of Chemical Physics* **131**, Article No. 134705 (2009).

[16] J. J. Juárez, J.-Q. Cui, B. G. Liu, and M. A. Bevan, kt-scale colloidal interactions in high frequency inhomogeneous ac electric fields. i. single particles, *Langmuir* **27**(15), 9211–9218 (2011).

[17] J. J. Juárez, B. G. Liu, J.-Q. Cui, and M. A. Bevan, kt-scale colloidal interactions in high-frequency inhomogeneous ac electric fields. ii. concentrated ensembles, *Langmuir* **27**(15), 9219–9226 (2011).

[18] J. J. Juárez and M. A. Bevan, Interactions and microstructures in electric field mediated colloidal assembly, *The Journal of Chemical Physics* **131**(13), Article No. 134704 (2009).

[19] J. J. Juárez, S. E. Feicht, and M. A. Bevan, Electric field mediated assembly of three dimensional equilibrium colloidal crystals, *Soft Matter* **8**(1), 94–103 (2012).

[20] T. D. Edwards, D. J. Beltran-Villegas, and M. A. Bevan, Size dependent thermodynamics and kinetics in electric field mediated colloidal crystal assembly, *Soft Matter* **9**(38), 9208–9218 (2013).

[21] T. L. Hill, A different approach to nanothermodynamics, *Nano Letters* **1**(5), 273–275 (2001).

[22] T. L. Hill, Perspective: nanothermodynamics, *Nano Letters* **1**(3), 111–112 (2001).

[23] R. S. Berry, Thermodynamics: Size is everything, *Nature* **393**(6682), 212–213 (1998).

[24] R. Berry, The amazing phases of small systems, *Comptes Rendus Physique* **3**(3), 319–326 (2002).

[25] H. Risken, The fokker-planck equation: Methods of solution and applications, 2nd ed. (1996).

[26] C. W. Gardiner, *Handboook of Stochastic Methods for Physics, Chemistry, and the Natural Sciences, 2nd ed.* (Springer-Verlag, Berlin, 1985).

[27] N. G. Van Kampen, *Stochastic Processes in Physics and Chemistry, 3rd ed.* (North-Holland, Amsterdam, 2007).

[28] G. Hummer and I. G. Kevrekidis, Coarse molecular dynamics of a peptide fragment: Free energy, kinetics, and long-time dynamics computations, *The Journal of Chemical Physics* **118**(23), 10762–10773 (2003).

[29] D. I. Kopelevich, A. Z. Panagiotopoulos, and I. G. Kevrekidis, Coarse-grained kinetic computations for rare events: Application to micelle formation, *The Journal of Chemical Physics* **122**(4), Article No. 044908 (2005).

[30] D. I. Kopelevich, A. Z. Panagiotopoulos, and I. G. Kevrekidis, Coarse-grained computations for a micellar system, *The Journal of Chemical Physics* **122**(4), Article No. 044907 (2005).

[31] M. A. Amat, I. G. Kevrekidis, and D. Maroudas, Coarse molecular-dynamics determination of the onset of structural transitions: Melting of crystalline solids, *Physical Review B* **74**(13), Article No. 132201 (2006).

[32] M. A. Amat, I. G. Kevrekidis, and D. Maroudas, Coarse molecular-dynamics analysis of stress-induced structural transitions in crystals, *Applied physics letters* **90**(17), 171910–171910 (2007).

[33] M. A. Amat, M. Arienti, V. A. Fonoberov, I. G. Kevrekidis, and D. Maroudas, Coarse molecular-dynamics analysis of an order-to-disorder transformation of a krypton monolayer on graphite, *The Journal of chemical physics* **129**(18), 184106–184106 (2008).

[34] G. Hummer, Position-dependent diffusion coefficients and free energies from bayesian analysis of equilibrium and replica molecular dynamics simulations, *New Journal of Physics* **7**(1), 34 (2005).

[35] D. J. Beltran-Villegas, R. M. Sehgal, D. Maroudas, D. M. Ford, and M. A. Bevan, Fokker–planck analysis of separation dependent potentials and diffusion coefficients in simulated microscopy experiments, *The Journal of Chemical Physics* **132**, Article No. 044707 (2010).

[36] R. R. Coifman, S. Lafon, A. B. Lee, M. Maggioni, B. Nadler, F. Warner, and S. W. Zucker, Geometric diffusions as a tool for harmonic analysis and structure definition of data: Diffusion maps, *Proceedings of the National Academy of Sciences of the United States of America* **102**(21), 7426–7431 (2005).

[37] B. Nadler, S. Lafon, R. R. Coifman, and I. G. Kevrekidis, Diffusion maps, spectral clustering and eigenfunctions of fokker-planck operators, *arXiv preprint math/0506090* (2005).

[38] R. R. Coifman and S. Lafon, Diffusion maps, *Applied and Computational Harmonic Analysis* **21**(1), 5–30 (2006).

[39] B. Nadler, S. Lafon, R. R. Coifman, and I. G. Kevrekidis, Diffusion maps, spectral clustering and reaction coordinates of dynamical systems, *Applied and Computational Harmonic Analysis* **21**(1), 113–127 (2006).

[40] R. R. Coifman, I. G. Kevrekidis, S. Lafon, M. Maggioni, and B. Nadler, Diffusion maps, reduction coordinates, and low dimensional representation of stochastic systems, *Multiscale Modeling & Simulation* **7**(2), 842–864 (2008).

[41] A. L. Ferguson, A. Z. Panagiotopoulos, I. G. Kevrekidis, and P. G. Debenedetti, Nonlinear dimensionality reduction in molecular simulation: The diffusion map approach, *Chemical Physics Letters* **509**(1), 1–11 (2011).

[42] R. R. Coifman, Y. Shkolnisky, F. J. Sigworth, and A. Singer, Graph laplacian tomography from unknown random projections, *Image Processing, IEEE Transactions on* **17**(10), 1891–1899 (2008).

[43] D. P. Huttenlocher, G. A. Klanderman, and W. J. Rucklidge, Comparing images using the hausdorff distance, *Pattern Analysis and Machine Intelligence, IEEE Transactions on* **15**(9), 850–863 (1993).

[44] A. L. Ferguson, A. Z. Panagiotopoulos, P. G. Debenedetti, and I. G. Kevrekidis, Integrating diffusion maps with umbrella sampling: Application to alanine dipeptide, *The Journal of chemical physics* **134**, Article No. 135103 (2011).

[45] A. L. Ferguson, A. Z. Panagiotopoulos, P. G. Debenedetti, and I. G. Kevrekidis, Systematic determination of order parameters for chain dynamics using diffusion maps, *Proceedings of the National Academy of Sciences* **107**(31), 13597–13602 (2010).

[46] F. Oosawa and S. Asakura, Surface tension of high-polymer solutions, *The Journal of Chemical Physics* **22**(7), 1255–1255 (1954).

[47] N. F. Carnahan and K. E. Starling, Equation of state for nonattracting rigid spheres, *The Journal of Chemical Physics* **51**(2), 635–636 (1969).

[48] D. J. Beltran-Villegas and M. A. Bevan, Free energy landscapes for colloidal crystal assembly, *Soft Matter* **7**(7), 3280–3285 (2011).

[49] D. J. Beltran-Villegas, R. M. Sehgal, D. Maroudas, D. M. Ford, and M. A. Bevan, Colloidal cluster crystallization dynamics, *The Journal of Chemical Physics* **137**, Article No. 134901 (2012).

[50] D. J. Beltran-Villegas, R. M. Sehgal, D. Maroudas, D. M. Ford, and M. A. Bevan, A smoluchowski model of crystallization dynamics of small colloidal clusters, *The Journal of Chemical Physics* **135**, Article No. 154506 (2011).

[51] P. R. ten Wolde, M. J. Ruiz-Montero, and D. Frenkel, Numerical calculation of the rate of crystal nucleation in a lennard-jones system at moderate undercooling, *The Journal of Chemical Physics* **104**, Article No. 9932 (1996).

[52] M. A. Bevan, D. M. Ford, M. A. Grover, B. Shapiro, D. Maroudas, Y. Yang, R. Thyagarajan, X. Tang, and R. M. Sehgal, Controlling assembly of colloidal particles into structured objects: Basic strategy and a case study, *Journal of Process Control* **27**, 64–75 (2015).

[53] T. D. Edwards, Y. Yang, D. J. Beltran-Villegas, and M. A. Bevan, Colloidal crystal grain boundary formation and motion, *Scientific Reports* **4** (2014).

[54] J. J. Juárez, P. P. Mathai, J. A. Liddle, and M. A. Bevan, Multiple electrokinetic actuators for feedback control of colloidal crystal size, *Lab on a Chip* **12**(20), 4063–4070 (2012).

[55] D. R. Nelson and B. Halperin, Dislocation-mediated melting in two dimensions, *Physical Review B* **19**(5), Article No. 2457 (1979).

[56] Y. Yang, R. Thyagarajan, D. M. Ford, and M. A. Bevan, Dynamic colloidal assembly pathways via low dimensional models, *The Journal of Chemical Physics* **144**(20), Article No. 204904 (2016).

[57] R. M. Sehgal, J. G. Cogan, D. M. Ford, and D. Maroudas, Onset of the crystalline phase in small assemblies of colloidal particles, *Applied Physics Letters* **102**(20), 201905–201905 (2013).

[58] R. M. Sehgal, D. Maroudas, and D. M. Ford, Effects of the attractive potential range on the phase behavior of small clusters of colloidal particles, *Journal of Chemical & Engineering Data* **59**(10), 3105–3112 (2014).

[59] T. L. Hill, *Thermodynamics of small systems* (Courier Corporation, 1963).

[60] D. J. Earl and M. W. Deem, Parallel tempering: Theory, applications, and new perspectives, *Physical Chemistry Chemical Physics* **7**(23), 3910–3916 (2005).

[61] Q. Yan and J. J. de Pablo, Hyper-parallel tempering monte carlo: Application to the lennard-jones fluid and the restricted primitive model, *The Journal of Chemical Physics* **111**(21), 9509–9516 (1999).

[62] Q. Yan and J. J. de Pablo, Hyperparallel tempering monte carlo simulation of polymeric systems, *The Journal of Chemical Physics* **113**(3), 1276–1282 (2000).

[63] H. Fukunishi, O. Watanabe, and S. Takada, On the hamiltonian replica exchange method for efficient sampling of biomolecular systems: Application to protein structure prediction, *The Journal of Chemical Physics* **116**(20), 9058–9067 (2002).

[64] J. Savage and A. Dinsmore, Experimental evidence for two-step nucleation in colloidal crystallization, *Physical Review Letters* **102**(19), Article No. 198302 (2009).

[65] Y. Wang, Y. Wang, X. Zheng, É. Ducrot, J. S. Yodh, M. Weck, and D. J. Pine, Crystallization of dna-coated colloids, *Nature Communications* **6** (2015).

[66] J. S. Oh, Y. Wang, D. J. Pine, and G.-R. Yi, High-density peo-b-dna brushes on polymer particles for colloidal superstructures, *Chemistry of Materials* **27**(24), 8337–8344 (2015).

[67] J. M. Gibbs-Davis, G. C. Schatz, and S. T. Nguyen, Sharp melting transitions in dna hybrids without aggregate dissolution: Proof of neighboring-duplex cooperativity, *Journal of the American Chemical Society* **129**(50), 15535–15540 (2007).

[68] M. Dijkstra, R. van Roij, and R. Evans, Direct simulation of the phase behavior of binary hard-sphere mixtures: test of the depletion potential description, *Physical Review Letters* **82**(1), 117 (1999).

[69] X. Tang, B. Rupp, Y. Yang, T. D. Edwards, M. A. Grover, and M. A. Bevan, Optimal feedback controlled assembly of perfect crystals, *ACS Nano* (2016).

[70] D. J. Wales and J. P. Doye, Global optimization by basin-hopping and the lowest energy structures of lennard-jones clusters containing up to 110 atoms, *The Journal of Physical Chemistry A* **101**(28), 5111–5116 (1997).

[71] R. M. Sehgal, D. Maroudas, and D. M. Ford, Phase behavior of the 38-atom lennard-jones cluster, *The Journal of Chemical Physics* **140**(10), Article No. 104312 (2014).

[72] P. A. Frantsuzov and V. A. Mandelshtam, Size-temperature phase diagram for small Lennard-Jones clusters, *Physical Review E* **72**(3), 1–4 (2005).

[73] V. A. Mandelshtam and P. A. Frantsuzov, Multiple structural transformations in Lennard-Jones clusters: Generic versus size-specific behavior, *Journal of Chemical Physics* **124**(20), 1–11 (2006).

[74] R. M. Sehgal and D. Maroudas, Equilibrium shape of colloidal crystals, *Langmuir* **31**(42), 11428–11437 (2015).

[75] G. Wulff, Xxv. zur frage der geschwindigkeit des wachsthums und der auflösung der krystallflächen, *Zeitschrift für Kristallographie-Crystalline Materials* **34**(1), 449–530 (1901).